Assessing Mechanical Performance of Dissimilar Steel Systems Made Via Wire-Arc Additive Manufacturing

A Thesis Presented for the

Master of Science

Degree

The University of Tennessee, Knoxville

Obed Daniel Acevedo

December 2021

This is all for Paola and my family back home.

Acknowledgments

First, I would like to thank my advisor Dr. Sudarsanam S. Babu, who helped me get to where I am. His patience, guidance, and support allowed me to obtain the tools I needed to be successful, not just in research but also in life. He always went the extra mile to help me reach the next step, and I am genuinely thankful to have had him be my mentor throughout this time. I also want to thank the rest of my committee, Dr. Brett G. Compton and Dr. Eric A. Lass, whose guidance helped me reach the next level during my research. I also want to thank Dr. Gerald Egeland and Dr. John Bohling for their assistance and for providing me with all the resources I needed to perform my research at UTK.

Secondly, I would like to thank the research staff at the Manufacturing Demonstration Facility, especially Dr. Yukinori Yamamoto, Dr. Andrzej Nycz, Dr. Mark Noakes, and their team for providing me with the materials used in this study, as well as their guidance and support. I also want to thank Dr. Michael Kirka for his support during my initial stages in research and Dr. Patxi Fernandez-Zelaia for his guidance and mentorship, especially for teaching me how to use Python! I would also like to thank Andrés Marquez-Rossy for always going out of his way to help me with any characterization needs, believing in me, and keeping me out of trouble.

Thanks to my family back home, especially Isabel, Gardy, Obed, and Eddie, who always believed in me and always made sure I had everything I needed to succeed. Their unconditional support was incredibly important during this process. Te amo, Ma! I want to thank all my friends back home for always being supportive and cheering me on.

Last but absolutely not least, I want to thank Paola, the love of my life. Without you, I would never have gotten this far. Your never-ending love and support gave me strength when I needed it. Thank you for helping to keep going.

Abstract

Hot stamping is part of a specific type of metalworking procedure widely used in the automotive industry. This research seeks to help make hot stamp tooling component production more cost-effective by using large-scale additive manufacturing. Additive manufacturing can produce dissimilar steel components that can be more cost-effective and time-efficient and allow for complex geometries to be made. A dissimilar steel system consisting of 410 martensitic stainless steel and AWS ER70S-6 mild steel is proposed to make hot stamps, making them more cost-efficient. However, the material interface's mechanical behavior in 410SS-mild steel additively manufactured material systems is not well understood. This research seeks to find how these dissimilar hot stamps can potentially fail during service. To assess the mechanical behavior of the material interface, mechanical testing by way of hardness testing, thermal expansion testing, fatigue testing, and microscopic imaging were performed. Samples were heat-treated, and fatigue tests were designed to run for 1200 cycles at a temperature range of 200-600°C. Fatigue test results show that, as expected, all four samples went through plastic deformation, with hardness test results used to confirm this behavior. Microscopy was done to show the post-test microstructure that shows potential evidence of plastic deformation sites. One of the materials in the dissimilar system did not meet the hardness requirements for hot stamping applications, but recommendations are made to address this.

Table of Contents

1 Introduction **1**

1.1 Motivation . . . 2

2 Literature review **4**

2.1 Hot Stamping . . . 4

2.2 Additive manufacturing . . . 7

2.2.1 Powder Bed Systems . . . 9

2.2.2 Direct Energy Deposition Systems . . . 10

2.2.3 Cost Comparison Between Additive Manufacturing and Traditional Manufacturing . . . 11

2.3 Dissimilar Metal Systems . . . 12

2.4 Fatigue . . . 13

2.5 Scientific and Technical Gaps . . . 15

3 Objective **16**

3.1 Thesis Plan . . . 16

3.1.1 Define Conditions & Stamping Die Stress State . . . 16

3.2 Hypothesis . . . 18

4 Materials & Procedure **21**

4.1 410 Martensitic stainless steel . . . 21

4.2 Mild steel . . . 22

4.3 Procedure and Equipment . . . 23

4.3.1 WAAM part geometry . . . 23
4.3.2 Sample preparation and heat treatment . . . 24
4.3.3 Thermal expansion testing . . . 25
4.3.4 Optical Microscopy . . . 26
4.3.5 Hardness testing . . . 27
4.3.6 Thermomechanical Fatigue Testing . . . 27

5 Results and Discussion **29**

5.1 Thermal expansion testing . . . 29
5.2 Fatigue testing . . . 31
5.3 Microscopy . . . 32
5.4 Hardness testing . . . 33

6 Summary and Conclusion **37**

6.1 Summary . . . 37
6.2 Conclusion . . . 38

Bibliography **39**

Appendices **47**

A Figures . . . 48
B Figures (cont.) . . . 68
C Tables . . . 74

Vita **76**

List of Tables

1 22MnB5 composition 74
2 410 martensitic stainless steel composition 74
3 Mild steel composition steel composition 74
4 Material Properties 74
5 Deposition parameters 75

List of Figures

1 Sample used for hammer experiment. 48

2 Patterns indicating possible flow lines after being struck with hammer. . . . 48

3 Different parts geometries made via hot stamping for automotive applications 49

4 Typical formed shapes in hot stamping. a) Singly curved; b) stretch flange; c) shrink flange; d) curved sections; 3) deep-drawn cup; f) beaded section [1] 49

5 Time-Temperature-Transformation diagram for 25Mn5B boron steel [2] . . . 50

6 Temperature-dependent flow curves for 22MnB5 boron steel [2] 50

7 Powder-bed deposition cycle [3] 51

8 Break even point for High-Pressure Die Casting and Selective Laser Sintering [4] 51

9 Contact surfaces between stamp and worksheet [5] 52

10 Stress element on surface of the die stamp 52

11 410 SS predicted hardness values over time in four temperature ranges . . . 53

12 410 SS predicted hardness values for 6.4 hours at 600°C 54

13 Iron-Chromium system phase diagram 55

14 WAAM part used in this study 56

15 WAAM part dimensions 56

16 Dimensions for sectioned bars 57

17 Sample schematic for thermal expansion testing 57

18 Samples sectioned from wall 58

19 Sample schematic for optical microscopy and hardness testing 58

20 Samples dimensions used for fatigue testing 59

21 Sectioned gleeble samples after testing 59

22 TA Q400 thermomechanical analizer 59
23 Raw CTE data showing plot of dimensional change as a function of temperature 60
24 Cr mapping along dissimilar sample interface 60
25 Test setup in the Gleeble 1500 61
26 CTE test results 61
27 Resolved stress element considering thermal stresses along σ_2 and σ_3 62
28 Stress-Strain results plot for sample 1 62
29 Stress-Strain results plot for sample 2 63
30 Stress-Strain results plot for sample 3 63
31 Stress-Strain results plot for sample 4 64
32 Force-time results plot for sample 1 64
33 Force-time results plot for sample 2 65
34 Force-time results plot for sample 3 65
35 Force-time results plot for sample 4 66
36 Sample 1 experimental temperature vs programmed temperature profile . . . 66
37 Sample 2 experimental temperature vs programmed temperature profile . . . 66
38 Sample 3 experimental temperature vs programmed temperature profile . . . 67
39 Sample 4 experimental temperature vs programmed temperature profile . . . 67
40 Microstructure comparison between as-printed sample (above) and heat-treated sample (below) 67
41 Delta ferrite grains in the as-printed condition 68
42 Sample 1 interface region microstructure after fatigue testing at 100x magnification 69
43 Sample 2 interface region microstructure after fatigue testing at 100x magnification 69
44 Sample 3 interface region microstructure after fatigue testing at 100x magnification 70
45 Sample 4 interface region microstructure after fatigue testing at 100x magnification 70
46 As-printed sample hardness map 71

47 Heat-treated sample hardness map 71
48 Hardness histogram comparison 72
49 Hardness comparison between tested samples over distance 72
50 Hardness histogram for fatigue-tested samples 73

Chapter 1

Introduction

Hot stamping is part of a specific type of metalworking procedure known as deep-drawing that is widely used in the automotive industry and allows for automated mass production of body components. This technology's advantage is that high-strength, lightweight components can be produced at a high rate at a low-cost [6]. This research seeks to help make hot stamp tooling component production more cost-effective and time-efficient using additive manufacturing (AM). Current manufacturing methods, such as forging or casting, make components that can withstand temperatures of up to 600°C and stresses between 200-700 MPa [7]. 410 martensitic stainless steel is a suitable material as it can easily form martensite and meet hot stamp tooling hardness requirements. However, this process can be expensive and time-consuming. Additive manufacturing can produce dissimilar steel components that can be more cost-effective and time-efficient and allow for complex geometries like cooling channels to be made. The material interface's mechanical behavior in 410SS-mild steel additively manufactured material systems is not well understood. Very little research is found in the literature, except for Tenuta et al. [8] where they studied the dissimilar metal system in the as-printed condition. They printed three 410SS-MS builds using different tool path configurations using wire-arc additive manufacturing and found no significant difference in strength when changing tool path parameters. The study also showed that different microstructures developed along the interface and the mild steel with different parameters.

Initial experimentation using crude methods explained in the next section provided insight that led to more sophisticated testing methods like thermomechanical testing under hot stamping conditions. This research will focus on the fatigue performance of dissimilar AM samples made up of 410 martensitic stainless steel and mild steel considering hot stamping applications.

1.1 Motivation

Hot stamping is a technology that has been implemented since the 1970s, initially for saw blades and lawn mower blades [9]. In 1984, SAAB first used this process to manufacture automotive structural components [10]. This method allowed production to increase from 3 million parts per year to 107 million in 30 years [11]. Despite still being a popular method for mass automotive component production, current demands in CO2 reduction and increased vehicle efficiency calls for optimization in all aspects of automotive hot forming processes, such as hot stamp tool optimization and workpiece material optimization as well [12]. One approach to optimizing the hot stamp tool is reducing tool production costs without compromising tool performance. One alternative to reduce tool costs was exploring additive manufacturing and its production capabilities for technical and economic reasons such as higher part production rates and decreased material waste [13]. Additive manufacturing (AM) can produce parts of complex geometry in the same amount of time that it would require to produce a component with simple geometry with less material waste[14], with the addition that it can produce functionally graded components. This capability is crucial since hot stamp tools are usually cast high-temperature stainless steels that can be expensive to produce. With additive manufacturing, it is possible to produce high-strength steel parts in critical areas, such as the stamp's face, and non-critical areas can be made up of cheaper low alloy steels like mild steel. This can potentially reduce hot stamp tools costs in materials alone when comparing the costs of mild steel and 410 stainless steel. The economics of AM will be discussed in more detail in the next chapter.

An interesting way to approach the question "how can an additively manufactured hot stamp fail?" was proposed during the discussions that led to this study. Due to the lack of literature regarding dissimilar steel fatigue testing, an interesting experiment was performed. The experiment consisted of heating a piece of additively manufactured printed dissimilar steel wall sample and simply hitting it with a hammer to see if and how the piece would deform. The initial hypothesis was that it would deform through the mild steel component of the sample. This is due to the mild steel having less yield strength than the 410 stainless steel components of the sample. To test this theory, the sample was placed in a furnace and heated to 450°C for an hour. The sample was then placed on an anvil and struck with a hammer with force being applied perpendicular to the material interface, as it would be during service in a hot stamp as shown in fig 1.

After striking the sample, the surface was polished to observe any anomalies that might have occurred. Fig. 2 shows that the interface seems to have deformed in the mild steel side (bottom). Mild steel has a yield strength of 378 MPa, whereas 410SS has a yield strength of 937 MPa at room temperature, meaning that the mild steel will plastically deform much earlier than the 410SS. Aside from the deformation observed, voids seem to be present at the interface where the weld beads end, but this was observed before the experiment began. Unfortunately, it would prove extremely difficult to measure the force of the hammer blows to measure the stresses applied. Even so, the experiment showed that the part deformed on the mild steel first. In fig. 1, it can also be observed a crack forming at the top right of the image where two beads are joined. This seems to have acted as a stress concentration area which reiterates the need for thorough surface finishing as it is extremely important for increasing component lifetime. On the mild steel side, patterns that possibly show the direction in which the mild steel deformed can be observed, which would mean the material did deform after being struck with the hammer on the mild steel side, as seen in fig. 2.

Chapter 2

Literature review

2.1 Hot Stamping

Hot stamping is divided into two processes, direct hot stamping and indirect hot stamping. Direct hot stamping occurs when a steel workpiece is heated and transferred to the stamp to be conformed to shape and quenched. In contrast, indirect hot stamping involves using a pre-shaped part placed on the hot stamp primarily for quenching, which is not considered in this research [11]. Fig 3 shows automotive structural components that make up a car, from simple rail-like components such as bumpers to complex shaft reinforcement components. These parts have different functions throughout an automobile. The different geometries that are possible to make with hot stamping are too many to specify. However, Sachs has divided sheet metal parts into five categories: single curve parts, contoured flanged parts, curved sections, deep-recessed parts, and shallow-recessed parts, as shown in fig 4.

It is essential to understand the conditions to which stamp tool materials are exposed to determine the property requirements for the materials that will make up the tool. When the stamp first comes into contact with the metal sheet, it is exposed to shearing forces along its edges. As the stamp fully presses the metal sheet, it is exposed to compression forces due to the bending of the metal sheet, which experiences tensile forces on one side and compressive forces on the other side, which is exposed to the stamp [1]. Throughout the process, the hot stamps are exposed to thermo-mechanical conditions, with thermal loads in a temperature range of 200-600° and mechanical loads ranging from 200 MPa to 700 MPa when exposed to the hot boron sheets at 900°C [7]. 22MnB5 is ultrahigh-strength boron-alloyed steel with flow stresses below 250 MPa at 950°C [7]. After the sheets are transferred to the stamp and pressed to conform it to the desired part geometry, the sheet is quickly cooled down at a rate of 27-100°C/s for approximately 20 seconds. This allows for martensitic transformations to occur, increasing the strength of the final part up to 1500 MPa [7]. Ideally, the load and temperature distribution would be equal along the entirety of the stamp, with a temperature deviation of ±5°C, but factors such as part geometry and cooling channel location present challenges. Traditional manufacturing methods, like machining, pose limitations as this does not allow cooling channels to conform to specific part geometries fully. These must be drilled or machined into the stamp, causing certain areas of the part to experience slower cooling rates that result in microstructural heterogeneity.

Materials used as hot stamping tools are expected to have yield strengths of up to 900 MPa, tensile strengths of up to 1200 MPa, and fatigue life of up to 10^4 life cycles to withstand high-temperature thermomechanical conditions from 200°C up to 600°C [11],[15], [16]. Medvedeva et al. performed a study with three tool steel alloys to try and increase temper resistance at high temperatures. The study showed that the alloy with the higher Mo and lowest Cr content showed the best tempering resistance [17]. Temper resistance is a material's ability to retain hardness and strength after tempering. When tempering a material, brittle microstructures, such as martensite, are eliminated by having carbon atoms diffuse out of the crystal lattice, developing more ferritic structures that result in a tougher material at the cost of some hardness. The brittle microstructures can be eliminated by having good tempering resistance, and the material can still retain more favorable mechanical properties [18]. Ghadar et al. performed a study comparing 410 stainless steel with K100 tool steel, both of which have similar chemical composition except C content. Hot deformation behavior was studied and compared between the two alloys where K100 showed higher carbide content due to higher C content and higher activation energy required for plastic deformations mechanism to activate [19]. Higher activation energy means that higher temperatures are required for a material to start deforming [20]. 410 is a high Cr martensitic stainless steel that can easily obtain a martensite structure after heat treating

[2], attaining desirable properties for hot stamping applications. 410SS will be discussed in further detail in chapter 4.

Various process variables must be considered in the hot stamping process, such as the time-temperature-transformations curves, flow curves, friction coefficients, and heat transfer coefficients for both the die stamp and workpiece materials. Time-temperature-transformation curves like fig. 5 show what phases can be expected during heat treatment of material depending on the cooling rate that the material is subjected to [11]. Fig. 5 shows that for 22MnB5 steel to attain a martensitic microstructure, a cooling rate of at least 30°C/s would be needed. Flow curves describe the stress-strain behavior and whether the material hardens or softens during tensile stress as observed in 6. Strain rate shows the rate at which a material is deformed, where higher strain rates cause higher flow stress values as stated by Dieter [1], and can cause brittle failure [21].

It is known that hot stamping tools fail during service due to wear, fatigue, and cracking, as stated in [11],[16]. Failure via plastic fatigue occurs due to plastic deformation brought about by cyclic thermomechanical loading during the stamping process. Areas of high-stress concentration, where the material's yield strength is exceeded, go through plastic deformation. This happens when the area where the mechanical loads are applied is significantly reduced, causing a significant increase in stress. Crack nucleation sites can originate in the stamp's corners and any voids present in the material due to the manufacturing process or elemental segregation [22], [23]. Fatigue life for hot stamps has been observed to be typically from 10^4 to 10^5 cycles when stresses applied can reach up to 700 MPa at temperatures of 650°C [24], [25], [6]. Fatigue life at these cycles is typically referred to as low-cycle fatigue. This research will focus on fatigue failure in hot stamping tool components by way of plastic deformation.

Hot stamping tools have been traditionally produced by casting and finished using traditional machining methods. Repairs or preventative maintenance can be done on hot stamps using tungsten inert gas wire [11], laser cladding, or even direct energy deposition [26], where an energy source melts metal in powder form in the area that needs to be repaired. Laser cladding is when a laser beam is used to melt a filler material to fuse it onto a substrate. This process can even be considered additive manufacturing (AM) if the filler material is used to create a near-net-shaped part [27]. Tungsten inert gas wire welding (TIG) is a direct-energy deposition process where a steel wire is fed through a nozzle and is melted using an electric arc by using a tungsten electrode inside an inert shielding gas such as argon or helium. This method allows for precise welds free of spatter and can weld almost all metals [27]. This process is expensive, however, and requires a high skill level from the operator to avoid issues such as overheating and oxidation.

2.2 Additive manufacturing

Welding has long been a significant part of human history and a fine example of human ingenuity since the Bronze Age up until today [Milewski, 2017]. The definition of welding, according to the American Welding Society (AWS), is "a joining process that produces coalescence of materials by heating them to a suitable temperature, with or without the application of pressure, and with or without the use of filler metal [AWS 1989]. There are over 50 defined methods of welding, according to the AWS [AWS 1989]. Out of all these, five have been adapted in the field of metal AM; laser beam welding (LBW), electron beam welding (EBW), gas metal arc (GMAW), gas tungsten arc (GTAW), and plasma arc (PAW) [DebRoy, 2018].

Additive manufacturing is developing technology with growing interest in the manufacturing industry. AM allows for the construction of three-dimensional parts via layer deposition, guided by a computer model. This allows for the fabrication of complex parts that are not possible by traditional subtractive manufacturing. Production time is significantly reduced during AM as there are fewer machining steps involved. Industries of interest in AM are aerospace, automotive, medical, and any other industry requiring components with complex geometry. While AM was initially developed for rapid prototyping using polymers as feedstock material by Chuck Hull in 1983, metal additive manufacturing became an area of great interest as it presents a viable option for mass production of parts [28]. Metal AM was initially developed from powder metal technology in the 1980s using selective laser sintering [29].

It is important to identify which material is best suited for each application [30]. Each class of materials presents its own unique set of challenges that go hand in hand with the application to be studied. Not only does the material have to be considered, but the actual AM method as well. Multiple studies concerning the printability of various metals for large-scale metal AM processes have been carried out with materials like Ti-6AL-4V. Bobbio et al. presented work involving additive manufacturing of functionally graded builds composed of Ti-6Al-4V with INVAR by using computer models to predict phase formation to understand whether any detrimental phases would form and if these would cause the material to fail [31]. Another study was performed by Blackwell, where the feasibility of producing laser-deposited Inconel718 (IN718) was evaluated [32]. The study showed that IN718 was successfully printed as the material showed comparable mechanical properties to its wrought counterpart. Tensile and yield strengths were shown to be 1436 MPa and 1257 MPa, respectively, while the wrought part showed tensile and yield strengths of 1365 and 1125 MPa, respectively [32]. This is possible because the high level of heat source control that AM provides allows for the control of cooling rates that enable preferential solidification conditions similar to casting. By enabling the development of longitudinal grains along the solidification direction, parts processed via AM can attain similar microstructure, and therefore, comparable mechanical properties to their cast counterparts. The materials considered for this study are discussed in chapter 4.

High cooling rates of 27°C/s that allow quenching of the stamped metal sheets are achieved by using cooling channels that go through the stamp, using water as coolant [33]. Cooling channels are critical for optimal hot stamp performance, but unfortunately, traditional manufacturing methods like casting or machining do not allow for optimal cooling channel geometry to be implemented without compromising part integrity [34]. Depending on the final part's geometry, subtractive manufacturing limitations do not fully allow cooling channels, components that are essential in hot stamps, to conform to specific part geometries. They must be drilled into the stamp, causing some regions of the part to experience slower cooling. Cooling channels must be drilled in, or the stamps must be assembled to integrate them into the stamp. This means that heat extraction is uneven if the channels are not conformed to the part's geometry. Varying heat fluxes throughout a die stamp can cause heterogeneous microstructural development that results in different mechanical properties throughout the part, severely affecting part integrity and performance. Muvunzi et al. have proposed a method to design cooling channels using additive manufacturing. Their work shows how to specify build parameters depending on part geometry and whether it is viable to apply conformed cooling channels as not all parts would require these. They compared cooling scenarios with conformed cooling channels and non-conformed cooling channels. Conformed cooling channels are channels whose path is conformed to the part's surface geometry, allowing for uniform heat extraction. Non-conformed cooling channels are typically drilled into the part regardless of variations along the surface geometry. The study showed that the conformed cooling channels' more uniform heat extraction allowed for the part to reach desired hardness values of 400 HV within 5 seconds, while the non-conformed cooling channels caused the part to reach the desired hardness value within 9 seconds, showing a potential decrease in part cooling time by 55% [35].

Additive manufacturing allows for fast production of parts without considering geometry complexity, as it takes the same amount of time to make a simple part longer than it would take to make a significantly more complex part. A 30 lb near-net shape part can be built in an hour on a large-scale AM system, according to Nycz [13]. Not only does AM present little difficulty in making complex parts, but it can also reduce the number of components needed for a part. One example is a Strati vehicle model produced via AM. The vehicle traditionally has over 20,000 components, but a redesign done using AM, the new model consisted of only 50 components. With AM, it is possible to produce dissimilar die stamps with conformed cooling channels without the need to drill them into the stamp. The printed part would be made entirely with just one component and would only need heat treatment and surface finishing. In theory, with a large enough build envelope, multiple stamps can be manufactured simultaneously, even when using multiple materials in a single part.

2.2.1 Powder Bed Systems

Powder bed systems are additive manufacturing systems where layer-by-layer metal powder deposition occurs. This is done by first having a CAD model of the desired part, which indicates the path that a heat source such as a laser or an electron beam will take. The eat source will melt the powder in its path. After the layer has been melted, the build volume will lower to allow for a new layer to be made until the build volume is completed. Three technologies currently make up powder bed fusion systems, these being selective laser sintering (SLS), selective laser melting (SLM), and electron beam melting (EBM). In SLM and SLS systems, layer-by-layer deposition occurs within an inert atmosphere to avoid fast oxidation [36]. In EBM, however, deposition occurs in a vacuum to avoid electron scattering from the beam [30]. Figure 7 shows the steps that happen during the deposition of a single layer [3]. After melting and completing a layer, the build volume is lowered, and rakes distribute powder to make a new layer until part deposition is completed. Powder bed systems are ideal for parts possessing significantly complex geometries. This process, however is better suited for smaller with dimensions under 3 feet along the largest axis, as these systems are not yet able to produce parts at the volume of large scale systems found in direct energy deposition systems.

2.2.2 Direct Energy Deposition Systems

Direct energy deposition (DED) systems function differently from powder bed systems in the way they add material on a layer-by-layer basis. Powder bed systems fill an entire layer with the material while the heat source melts material along the deposition path. On the other hand, DED deposits material only along the path where deposition happens by depositing material directly into the heat source. DED is classified into two categories: powder feed and wire feed systems. During the powder feed process, a heat source such as a laser creates a melt pool along its scan path while material powder is fed through a nozzle directly into the melt pool [12]. A wire-feed system works similarly to the powder-fed system, except the material is fed through a nozzle into an electric arc that serves as a heat source. This process is very similar to traditional welding methods [12]. Three methods rely on the same principle within wire-fed systems, with the heat source being the difference. These methods are wire-laser additive manufacturing (WLAM), electron beam additive manufacturing (EBAM), and wire arc additive manufacturing (WAAM) [12]. This study will focus on materials deposited using WAAM.

Wire arc additive manufacturing (WAAM) is a metal additive technique adopted from traditional gas metal arc welding (GMAW) techniques that use an electric arc discharge as a heat source and metal wire as feedstock [Williams-Sames]. The electric arc melts a substrate where the feedstock wire is then deposited while an automated robotic arm controls the system's motion. According to Nycz, WAAM technology currently can build metal components at a deposition rate of up to 30 lbs/h. In theory, its potential is limitless as these systems can be easily adjusted to further increase deposition rates as more robotic arms with wire feeding nozzles for deposition are added [13]. WAAM systems also show significant potential for scaling up than other AM methods like powder bed systems for various reasons. For example, a wire-arc system only requires an envelope of protective inert gas, making for a significantly less complex environment that can be expanded [13]. While it is possible to scale up a powder bed system, it is more restrictive because it requires a volume increase in the vacuum chamber that powder bed systems possess.

2.2.3 Cost Comparison Between Additive Manufacturing and Traditional Manufacturing

AM is well known for having extremely low buy-to-fly ratios. The buy-to-fly ratio is a ratio that considers the weight of a material billet that will be used for making a part and the weight of the final part itself. For a 10:1 ratio, a billet was reduced to just 10% of its original weight to obtain the final part. Traditional subtractive manufacturing has been known to have buy-to-fly ratios from 10:1 to 40:1 [37], [38]. With AM, however, buy-to-fly ratios of 3:1 to almost 1:1 are possible [39]. One pound of mild steel costs around 4 dollars, and one pound of 410 stainless costs around 7.5 dollars. If one 100lb. hot stamp component is reduced to 50% stainless steel, the cost of materials is reduced by 24%. This is because additive manufacturing produces 98% less material waste than traditional manufacturing methods [12].

In a study by Atzeni and Salmi, it was shown that Selective Laser Sintering could be more cost-effective than Die-casting if the production volume were below 42 units, in which die-casting becomes more cost-effective [4]. An AM part can cost 617 dollars, but a die-cast part would cost 24,700 dollars, including the die mold for casting. As the number of components increases, die-casting becomes more cost-efficient, as seen in 8. This is a direct comparison only between the technologies' production costs. Additive manufacturing allows for cost advantage in hidden areas of inventory and supply chain costs [40]. One example is that, as previously mentioned, AM allows for a reduction in assembly time as fewer components are required with AM parts. This is also beneficial for reducing transportation costs and reduction in revenue time [40].

A case for WAAM being an optimal technology for making hot die stamps can be made. The first argument is made by defining if hot stamping falls within the large-scale additive manufacturing realm. Nycz et al. define large scale by having the longest axis length of a part be a minimum of 3-6 feet [13]. Considering that some parts made via hot stamps can have dimensions of up to 4 or 5 feet, such as automotive structural components, WAAM is able to provide a build volume large enough for deposition, and therefore hot stamping fits this criterion. The current maximum print envelope is 20' x 8' x 6'[13], but as stated previously, it can produce parts much larger if the addition of neighboring systems and more robotic arms are added [41]. Another factor to consider is the ease of raw material acquisition. As the two major feedstock types in metal additive systems are wire and powder, metal wire is far easier to obtain and cheaper than metal powder [42]. Aside from the costs and availability, the metal wire comes in many compositions readily available compared to much fewer alloys in powder form. The prices of commercial metal 3D printers start at about \$100k - \$500k. The larger the printer build volume, the more it costs [13]. One of the most important factors with these systems is the ability of the device to pay for itself, for which printing speed is the main factor. The more parts it can manufacture per unit of time, the faster it can pay for itself [13].

2.3 Dissimilar Metal Systems

With the addition of additive manufacturing for optimization of hot stamping components, particular challenges arise that must be understood to implement this technology successfully. Additive manufacturing itself poses a challenge in the sense that it is a relatively new technology. Certain aspects are not well understood, such as the mechanical properties of the mixed zone in some dissimilar steel materials, which is the case for a 410SS-mild steel system. This means that little information can be used as a baseline when analyzing and characterizing these material systems.

One particular challenge when working with dissimilar materials is thermal mismatch [43]. If two metals have significantly different thermal expansion coefficients, failure at the material interface could occur due to shearing forces [44]. In this study, there was a concern regarding the mismatch in CTE, so a study was made. This study is discussed in detail in chapter 4, and the results are discussed in chapter 5.

2.4 Fatigue

Fatigue is defined as a process of damage and failure due to cyclic loading [45]. Fatigue is a subject of extreme importance in engineering design as it is one of the most common causes of fracture. From bridges to automobiles, fatigue must be considered thoroughly in the performance life of any device exposed to cyclic loading conditions such as vibration or repeated loading [45]. 80% of the economic costs of fracture failure occurrence and prevention involve cyclic loading and fatigue in some form. The annual cost of material fatigue in the US economy is about 3% of the gross national product (GNP). These costs arise from the occurrence of fatigue or from developing methods of fatigue prevention [45].

Fatigue is divided into two types, depending on the number of loading repetitions or cycles. These types are high cycle fatigue, where the number of repetitions can be over a million, and low cycle fatigue, where the number of repetitions can be in the hundreds or thousands. One thing to observe from these types of fatigue is that high cycle fatigue is usually associated with small amounts of deformation that are usually elastic, whereas low cycle fatigue is associated with large amounts of plastic deformation. If a material is exposed to cyclic heating and cooling, the resulting thermal stresses can cause what is known as thermal fatigue.

In many applications, cycling between maximum and minimum constant stress levels is known as cyclic loading. The difference between these values is called the stress range defined as $\Delta\sigma = \sigma_{max} - \sigma_{min}$. The average of these values is known as the mean stress or σ_m. The variation about the mean is known as the stress amplitude or σ_a. These definitions can be defined as

$$\sigma_a = \frac{\Delta\sigma}{2} = \frac{\sigma_{max} - \sigma_{min}}{2}, \quad \sigma_m = \frac{\sigma_{max+\sigma_{min}}}{2} \tag{2.1}$$

In a scenario where high-temperature exposure occurs, thermal stresses arise caused by the thermal expansion behavior of the materials. This means that, in this case, fatigue results from cyclic strain rather than cyclic stress. Hot stamps are exposed to low cycle fatigue during service, and even though this study will focus more on low cycle fatigue behavior, it is important to understand that both plastic and elastic deformation occurs during hot stamping [16]. Much work has been done to understand and predict fatigue behavior and the life of service components. One of the more popular methods is the Coffin-Manson equation

$$\frac{\Delta\varepsilon_p}{2} = \varepsilon'_f \left(2N_f\right)^c \tag{2.2}$$

where ε_p is the plastic strain amplitude, ε'_f is the fatigue ductility coefficient defined by the strain intercept at $2N_f = 1$, and c is the fatigue ductility exponent which varies between -0.5 and -0.7 for many metals [1]. This equation, however, does not consider elastic deformation, so another equation established by Basquin shows that

$$\sigma_a = \frac{\Delta\varepsilon_e}{2} E = \sigma'_f \left(2N_f\right)^b \tag{2.3}$$

where σ_a is the alternative stress amplitude, $\Delta\varepsilon_e/2$ is the elastic strain amplitude, b is the fatigue strength exponent, which varies between -0.05 and -0.12, and E is Young's modulus. These properties are easily attainable for any material from tensile test results. Dieter shows that it is possible to make an equation that is valid over the entire range of fatigue life by using superposition of eqs. 2.2 and 2.3 to obtain

$$\frac{\Delta\varepsilon}{2} = \frac{\sigma'_f}{E}\left(2N_f\right)^b + \varepsilon'_f\left(2N_f\right)^c \tag{2.4}$$

where $\Delta\varepsilon'_f/2$ is the amplitude strain, $2N_f$ is the number of load reversals, where one cycle equals two reversals, ε'_f and σ'_f/E are the points of intersection of the elastic and plastic curves with the axis when $2N_f = 1$; b and c are the inclinations of the elastic and plastic curves in logarithmic coordinates.

2.5 Scientific and Technical Gaps

Previous work has been done on dissimilar metal welding, which has proven helpful for research into the dissimilar AM fields. Niino proposed the concept of functionally graded materials (FGM) in 1987 by proposing the joining of NiCrAlY with ZrO2Y2O3 [46]. In 2015, Muller et al. proposed a modeling and system control designed for functionally graded materials deposited via direct laser powder deposition systems [47].

As previously mentioned, there is very little known work in the literature regarding the mechanical properties of a 410SS-mild steel interface made via WAAM. At the moment, the only work in the literature is that of Tenuta et al., who performed studies on 410SS/MS dissimilar systems at Oak Ridge National Lab (ORNL). The studies consisted of characterizing 410SS/MS samples by way of tensile testing with digital image correlation (DIC), electron backscatter diffraction (EBSD), and electron dispersive spectroscopy (EDS). Results showed tensile strengths of 506 MPa and yield strengths of 385 MPa were obtained. The results were consistent when testing samples with different print configurations and showed that the print pattern for the block did not have an effect on the mechanical properties of the materials [48]. The results also showed that deformation in the tested samples occurred in the mild steel, as per the DIC images showing the interface and all deformation occurring in the mild steel side.

Chapter 3

Objective

3.1 Thesis Plan

3.1.1 Define Conditions & Stamping Die Stress State

Understanding the stress state and loading conditions on a hot stamp during service requires that the workpiece metal sheet's conditions be understood as well. Workpieces are typically heated up to 950°C before they are worked into the desired geometry. This increase in temperature allows workpieces to be deformed by applying stresses as low as 200 MPa (ASMvol6). As the hot stamp comes into contact with the workpiece, shear stresses are exerted on the interface between the workpiece and the stamp, especially on the stamp corners, as seen in fig 9. Once the stamp is fully pressed down on the workpiece, there are both shear and a compressive force normal to the face of the die stamp.

In contrast, the workpiece is exposed mainly to tensile stresses. The direction of the shear forces is opposite to the direction in which the workpiece deforms or flows. The frictional forces are described using a constant coefficient of Coulomb friction

$$\mu = \frac{\tau}{\sigma} \tag{3.1}$$

where τ is the shear stress at the material interface, and σ is the stress normal to the stamp/workpiece interface. Once the workpiece is fully formed, compressive stresses are applied on the stamp's face, normal to the face of the workpiece.

Geiger performed tests using 22Mn5B boron steel sheets to determine the friction coefficient of these during service. The tests simulated a deep drawing process with a blank, a blank holder, and a drawing die at different temperatures from 500C to 850°C. The results showed that the friction coefficient on the test blanks decreased with increasing temperature, with coefficients values at around 0.38 with a blank temperature of 950°C and a tool temperature of 200°C.

For this study, some assumptions must be made to assess the stress state in a hot stamp. First, a stress element at the edge of a die stamp is evaluated. The corner of the die stamp is chosen because, as previously mentioned, it is the part of a stamp exposed to the highest mechanical loads. The second assumption is that uniaxial strain conditions are assumed. This assumption is made for the sake of performing a more simple yet still appropriate assessment. Uniaxial strain is a form of loading in which the principal axial component of strain ε_1 is nonzero, while all other strain components are zero. The stresses acting on the stamp are not readily known, so as an approximation, the yield stress in the 410 at 600°C is assumed to be equal to the von Mises stress such that

$$\sigma_{y,410SS@600^oC} = \sigma_0 = \frac{1}{\sqrt{2}}[(\sigma_x - \sigma_y)^2 + (\sigma_y - \sigma_z)^2 + (\sigma_z - \sigma_x)^2 + 6(\tau_{x_y}^2 + \tau_{y_z}^2 + \tau_{x_z}^2)]^{1/2} \quad (3.2)$$

To use the equation above for finding the loads on the stamp, on a three-dimensional stress element, the conditions assumed are

$$\sigma_1 \neq 0, \quad \sigma_2 = \sigma_3,$$

$$\varepsilon_1 \neq 0, \quad \varepsilon_2 = \varepsilon_3 = 0,$$

$$\tau_{12} \neq 0, \quad \tau_{23} = \tau_{31} = 0$$

$$\tau_{12} = \mu\sigma_1$$

With these assumptions, Hooke's Law for linear elastic behavior can be expressed as

$$\sigma_1 = \frac{(1-\nu)E\varepsilon_1}{(1+\nu)(1-2\nu)} \tag{3.3}$$

and

$$\sigma_2 = \sigma_3 = \frac{\nu\sigma_1}{(1-\nu)} \tag{3.4}$$

Hooke's Law equations for uniaxial strains allows the Von Mises stress equation to be expressed in terms of σ_1 such that

$$v.Mises = \frac{1}{\sqrt{2}}\left[\left(\frac{\nu\sigma_1}{1-\nu} - \sigma_1\right)^2 + \left(\sigma_1 - \frac{\nu\sigma_1}{1-\nu}\right)^2 + 12(\mu\sigma_1)^2\right]^{1/2} \tag{3.5}$$

where ν is Poisson's ratio, which for 410SS its value is 0.285. By assuming the von Mises stress to be equal to the yield strength of 375 in the 410SS at 600°C, σ_1 was calculated to be 338 MPa. Now, σ_2 and σ_3 can be calculated using Hooke's Law, which results in 135 MPa. The shear stresses were calculated using the previously mentioned Coulomb friction factor, and 128 MPa was obtained. There is a consideration with σ_2 and σ_3 regarding thermal stresses discussed in chapter 5. With this information, a fully resolved stress element is shown in fig. 10 to represent the loading conditions on the hot stamp. In the stress element, the stresses that do not show a value are assumed to be zero, as per the uniaxial strain analysis.

3.2 Hypothesis

This research seeks to understand how dissimilar materials joints made by wire-arc additive manufacturing perform under hot stamping conditions. As very little research has been done on 410SS-MS dissimilar systems except for Tenuta et al. [8],[48], so it could prove insightful to look into previous welding studies. However, even in welding studies, there is not much information regarding 410SS and mild steel welds. 410SS has a yield strength of

375 MPa at 600°C, the maximum service temperature that most hot stamps are exposed to when experiencing thermomechanical loading conditions. The steel system is going through conditions similar to tempering treatment throughout its service life, which leads to plastic deformation on the steel by way of yield strength reduction. This will cause it to plastically deform even when exposed to loading conditions initially within the material's elastic region.

To understand how the 410SS-MS system performs under hot stamping conditions, strains of 0.01% on the material, fatigue tests are designed to investigate the life cycle of a dissimilar hot stamp tool. After performing fatigue life prediction calculations and tempering response estimations, the mild steel is expected to fail at approximately 1200 cycles due to the material going through plastic deformation beyond the required geometrical tolerances during service. By using the Hollomon-Jaffe parameter, shown in eq. 3.6, which relates the variables of tempering time, temperature, material constant, and hardness, an estimation of the material's hardness can be made before and after service.

$$HJP = T(C + log(t)) \tag{3.6}$$

Where T is the temperature in Kelvin, C is a material constant with a value of 20 for most steels, and t is the tempering time in seconds. For 410SS, the Hollomon-Jaffe parameter can be related to hardness by using the relation shown in eq. 3.7 where

$$Hardness(HV) = -0.0161 * (T(C + log(t))) + 544.49 \tag{3.7}$$

This relation was established in the work of Kusunoki for a 410SS alloy composition similar to that of the one in this study [49]. Using this relation, predicted hardness values were calculated and shown in fig 11 at 200, 350, 550, and 600°C. Since these calculations have to be performed assuming isothermal conditions, multiple temperature ranges were estimated.

Hardness values were observed to range between 310 and 350 HV after heat treatment, and it is estimated to be 302 HV after 1200 cycles, or 6.4 hours of tempering time by using this parameter as shown in fig 12. This 17% decrease in hardness can be used to estimate a decrease in yield strength since hardness and yield strength are directly proportional to each other, as shown by Tabor [50]. After 6.4 hours, yield strength in the 410SS should have been reduced to approximately 311 MPa. In the case of the mild steel, the Hollomon-Jaffe parameter cannot be used as the relation established by Kusunoki only works with 410SS compositions, so other methods for approximations must be applied. Due to a lack of high-temperature data for mild steel, approximations were made with the work of Chen et al. They determined reduction factors for different mechanical properties, such a yield strength and Young's modulus, for various types of steels at high temperatures [51]. The authors showed that for mild steel, a reduction factor of 0.71 was appropriate. This is why an approximated yield strength of 110 MPa is assumed for mild steel at 600°C. Thus, the yield strengths of 410 and mild steel at 600°C are 375 MPa and 110 MPa, respectively. With this information, it is hypothesized that the samples are expected to deform plastically on the mild steel side. The 410SS is not expected to deform, but it will lose some of its yield strength.

Chapter 4

Materials & Procedure

4.1 410 Martensitic stainless steel

410 (410SS) is a high Cr martensitic stainless steel that can easily obtain a martensitic microstructure after heat treating [27]. Being able to reach yield strengths of up to 1220 MPa [15], hardness values of up to 43 HRC, and wear resistance of up to $1.38 \text{x} 10^{-4} \text{kg/m}^2\text{/h}$, obtained by way of slurry erosion tests [52], post-heat-treatment makes it a suitable candidate as a hot stamping tool material. Other applications for which 410 is suitable are valves, bearings, steam turbine blades, marine turbine blades, and compressor blades [53],[18].

AISI 410 stainless steel is the first low carbon martensitic stainless steel produced commercially [53]. This steel is highly favored for use in corrosive environments, and its high strength and resistance [53]. Previous studies on martensitic stainless steels have shown that as-welded parts possess microstructures in the form of δ-ferrite grains and untempered martensite laths in the form of $M_{23}C_6$ carbides, both of which are detrimental to the material's strength and toughness, respectively [54],[55]. While the δ-ferrite is very soft, untempered $M_{23}C_6$ carbides are very hard. This creates significant mechanical property heterogeneity. It has been reported that due to the saturation of ferrite stabilizing elements such as Cr, δ-ferrite can be retained at room temperature. One way to reduce these phases is to add austenite stabilizing elements like Ni and Mn, as reported by Stone et al. [56]. Stone et al. developed a predictive equation for the volume fraction of δ-ferrite that showed the quantification of alloy composition effects, demonstrating that it is possible to reduce

δ-ferrite formation during solidification and obtain fully martensitic microstructures upon cooling.

Depending on the material used, heat treatments are applied to the hot stamp tool materials to increase their durability. In the case of 410SS, these heat treatments usually consist of austenitization at 1050°C to eliminate deleterious phases as the previously mentioned δ-ferrite, a high-temperature ferrite phase stable at room temperature due to the presence of 12.5% Cr content in the 410SS as seen in fig 13. δ-ferrite has been shown to be extremely soft, which reduces the material's overall strength and creates mechanical property scatter [57]. This is followed by quenching in oil or water, causing martensitic microstructures to form, then tempering at 500-600°C from 1.5 to 2 hours to be either quenched again or air-cooled finally. With this heat treatment, Roy et al. showed that 410SS yield strength could be increased by 20%, from 784 MPa to 942 MPa, and a tensile strength increase of 8%, from 1135 MPa to 1226 MPa [15]. Martensite is formed in steels by the rapid cooling of austenite at such a high rate that carbon atoms do not have time to diffuse out of the (FCC) crystal structure in large enough quantities to form cementite. As a result of these high cooling rates, the face-centered cubic austenite transforms to a highly strained body-centered tetragonal (BCT) form called martensite [58], [15]. Martensite possesses higher strength and hardness than ferrite as it has higher elastic strain due to the trapped carbon atoms. Tempering allows some carbon atoms to diffuse out of the BCT structures and form carbides, increasing the material's toughness at the cost of reduced strength.

4.2 Mild steel

The mild steel used in this study is made with ER70S-6 wire. ER70S-6 is a copper-coated carbon steel wire suitable for automatic welding processes, and it is well known for its excellent weldability [59]. This alloy is used for piping and tubing, sheet metal, and pipe welding [59]. ER70S-6 was produced initially as a filler wire in gas tungsten arc welding (GTAW) applications. ER70S-6 composition is shown in table 3. ER70S-6 tensile properties have been studied at room temperature by Ermakova et al. In their study. They compared ER70S-6 with ER100S-1, similar low carbon steel with 1.5% Ni content. The results showed that ER70S-6 has a tensile strength of 520 and a yield strength of 378 MPa, while the ER100-1 showed a tensile strength of 817 MPa and a yield strength of 537 MPa [59]. Properties for 410SS and mild steel are shown in table 4

4.3 Procedure and Equipment

Understanding fatigue performance in 410SS/Mild steel dissimilar systems requires different material characterization tests. The experiments to be performed are as follows:

1. Sample preparation and heat treatment
2. Thermal expansion testing
3. Optical microscopy
4. Hardness testing
5. Fatigue testing

The studies are focused mainly on the macro properties of the material system. The procedure mentioned above should help establish further studies on this system. The testing performed is discussed in detail in the following sections.

4.3.1 WAAM part geometry

The part that was printed using WAAM for this study was an 8" x 6" x 4" steel block where half of the block consisted of 410SS and the other half consisted of mild steel, as shown in fig. 14, while fig. 15 shows the dimensions and sample location. Fig. 16 shows the dimensions for the bars sectioned from the block. The part was printed using the Wolf Robotics mBAAM system at the Manufacturing Demonstration Facility (MDF). The workspace is an enclosed and ventilated work cell with an ABB IRB 2600 robotic arm. This arm includes an IRC5 controller, a Lincoln Electric R500 Power Wave welder set to work in GMAW mode, and a dual push-pull wire feeder. The system allows for the use of different shielding gases such as Argon, CO_2, and Helium. The deposition parameters for the block are shown in table 5.

The wire used was the Lincoln Electric Blue Max MIG 410 (ER410) (Lincoln Electric Inc., Cleveland, OH, USA) with a 0.045-inch diameter for printing the 410SS. The Superarc L-59 wire (ER70S-6) with a 0.045 in. diameter was used for the mild steel. The arrows on fig 14 indicate the tool path.

4.3.2 Sample preparation and heat treatment

For thermal expansion testing, samples were sectioned from pieces of a previous multi-material build to make thermal expansion testing samples. This build was made using the same parameters as the more recent block. The build is a wall composed of 410 martensitic stainless steel, and the other half is composed of mild steel, as shown in fig. 17. Fig 18 shows three approximately 1" x 1.5" x 1" samples that were sectioned from this previous wall. The top and middle samples were subjected to a heat treatment that consisted of austenitization at 1050°C for 60 minutes. After austenitization, the bars were quenched in saltwater and then tempered at 550°C for 90 minutes, then water quenched. The bottom sample was left in the as-printed condition for comparison. From the as-printed sample, two smaller samples were prepared for thermal expansion testing as per the ASTM E831-19 standard procedure for linear thermal expansion testing. These samples are shown in fig. 17.

For microscopy and hardness testing, sectioning was done on the middle sample where a 0.25" x 1.5" x 0.25" strip was cut, and another strip with the same dimensions was cut from the top heat-treated sample. The two strips were mounted using Buehler KonductoMet® powder compound with a diameter of 2" and a height of 0.5" as shown in fig. 19. After mounting, the samples were ground and polished up to 1200 grit, followed by polishing using alumina compound. After polishing, a basic etchant consisting of 4% nital was used, but it could not reveal the microstructure on the 410SS surface. The ferrite grains in the mild steel were revealed very clearly, but this was not enough. Kalling's No. 2 reagent was used instead as this etchant was favorably revealed ferritic and martensitic microstructures in both the mild steel and the 410SS [60].

Samples for fatigue testing first were sectioned as shown in fig. 15 along with the 410SS-MS interface. Six bars were sectioned, followed by the same heat treatment described above. Sectioned part dimensions are shown in fig. 16. After heat treatment, the bars were machined into cylindrical gleeble specimens measuring 4.5" in length and 0.394" in diameter, as shown in fig. 20. The samples had a slight notch machined in the middle of the gage section to allow better heat conduction to the gage center during the tests. This notch measures 9.90 mm in diameter. Once the samples were machined, type K thermocouples were attached using the Gleeble 1500 thermocouple welder. To attach the thermocouples, the gauge length is measured to locate the center, and the wires are attached within 2mm from each other normal to the sample length. After testing, some concerns were raised regarding sample dimensions that will be discussed in the next chapter. Nevertheless, the tests and the results still provide significant insight into the materials' fatigue performance that has not been observed in large-scale AM dissimilar steel systems until this study. After testing was done, the samples were sectioned, as shown in fig. 21. These were polished and mounted using the same procedure as the microscopy samples for observation.

4.3.3 Thermal expansion testing

Over small temperature ranges, the linear nature of thermal expansion leads to expansion relationships for length, area, and volume in terms of the linear expansion coefficient using the relation

$$\alpha = \frac{\Delta L}{L_0 \Delta T} \tag{4.1}$$

where ΔL is the change in length along Z in the sample, L_0 is the initial length of the sample, and ΔT is the temperature change. Thermal expansion testing was performed using a TA Instruments Q400 thermomechanical analyzer shown in fig. 22. Samples were placed on the Q400 stage, and a probe was placed along the Z direction of each sample. The system was programmed to do a temperature ramp from 25°C up to 200°C at a ramp of 5°C/min. Four tests were performed for each material using the same parameters. The resulting raw data is shown as dimensional change in the sample as a function of temperature, as shown in fig. 23 .After data acquisition was complete, coefficients were obtained using the relationship shown in eq. 4.1 . This relationship essentially describes the slope of the temperature vs.

length displacement plot obtained in the tests divided by the initial length of the sample. With the raw data, a line fit is performed, and its line equation is obtained. Once the slope of the line is divided by the original sample length, the coefficient of thermal expansion (CTE) for that test run is also obtained. Once all the slopes and CTE values are calculated, a standard deviation for this new set of data points is obtained. An error can be extracted for each sample. Standard deviation and errors were calculated using the equations

$$standard\ deviation = \sqrt{\frac{\sum X_i - \overline{x}}{n-1}} \tag{4.2}$$

$$standard\ error = \frac{Standard\ deviation\ of\ the\ mean\ CTE}{\sqrt{number\ of\ tests\ per\ sample}} \tag{4.3}$$

where the standard deviation reflects the variability of individual data points, and the standard error is the variability of the slope means.

4.3.4 Optical Microscopy

Images were taken using a Leica DM4000 and Zeiss Axio Observer 5 light microscopes. Images were taken at 100x and 500x magnification at the material interface to observe microstructures in the as-printed, heat-treated, and post-test conditions. These images show microstructural changes that could occur after each stage of the part's processing stages. The images taken were stitched together to show the entirety of the surface that will allow microstructure evaluation along the interface of the materials. The interface can be assessed by performing image analysis with software such as ImageJ. In this work, however, the length of the interface was found by performing elemental mapping using energy dispersive spectroscopy to observe the extent of diffusion as shown in fig. 24.

4.3.5 Hardness testing

The hardness testing machine used was the Leco AMH55 110AT Hardness tester equipped with Vickers microindentation. The Vickers Pyramid Number [HV] was measured using a 300 gf load. For the as-printed set, 3,373 indents were made, making up a 33mm x 6mm grid with 250μm spacing between each indent in horizontal and vertical directions. A python code was written to show the indents along an "XY" grid, and by assigning their hardness values to create a color map, show the hardness distribution along the sample. This procedure was done on both the as-printed and heat-treated samples. After fatigue testing, the hardness in the samples was once again tested. For this procedure, a simple vector with 500 μm spacing between indents was used to make indents across the sample surface.

4.3.6 Thermomechanical Fatigue Testing

A Gleeble 1500 system was used to perform the thermomechanical fatigue testing. The system allows for complete control of thermal and mechanical test variables simultaneously through digital closed-loop thermal and mechanical servo systems. The Gleeble system can be operated totally by computer, fully manually controlled, or by any combination of the two needed to provide more flexibility in materials testing and physical simulation work. The environment for computer control of the Gleeble system consists of a Windows-based workstation that offers a Graphical User Interface for creating simulation programs, analyzing the resulting data, and creating reports and presentations. The embedded processor executes test and simulation programs and collects data under the control of the Windows program. This effectively enables the operator to create new tests and analyze data while actively executing tests or physical simulations. The operator can create tests on the workstation through several programming options. QuikSim Software is a spreadsheet-like, fill-in-the-blanks software that describes each action in a test sequence in order and duration. QuikSim allows arbitrary programming of waveforms for both thermal and mechanical systems [61]. The data is then processed using Origin, which allows for a complete analysis of the processed data.

The parameters for the tests performed in this study were chosen to simulate hot stamping conditions as closely as possible. The first parameter established was the temperature, where a range of 200°C to 600°C was set as this is the range of temperatures that hot stamps are exposed to during service, from pre-heating to stamping and subsequent quenching. The following parameters chosen were the loading conditions. There were some initial issues regarding the test setup, especially with the strain control parameters. The tests were first set up as strain-controlled fatigue tests with a strain amplitude of $1x10^{-4}$, but the system's resolution limits did not seem to allow measuring these strains correctly. A stroke-controlled procedure was done instead. After some calculations using constitutive relations, the stroke range needed to provide similar loading conditions as the strain-controlled tests went from 0 to -0.12 mm, enough to provide stresses in the range of 120 MPa, mostly in compression. A CGauge was used to measure sample diameter during testing. The CGauge is composed of a quartz rod with a spring that acts down on the rod to clamp the sample while taking measurements. Once the thermal and mechanical conditions loading conditions were set, a cycle time of 20 seconds was set, which is similar to the time it takes to form and quench a worksheet in service, for a total number of 1200 cycles, which is within a reasonable range of service lifetime. In the program script, the heat ramp is such that it takes 10 seconds to get from 200°C to 600°C. Unfortunately, quenching could not be simulated as the quenching system would likely damage the CGauge, this being an electronic component that would be damaged by the water used to quench, so air cooling was done. The results from this will be shown in chapter 5. The tests were programmed so that the maximum compressive stress occurs at the same time that the temperature reaches 600°C.

The test samples were placed in the system using copper grips to transfer heat and ramp up the temperature along the middle of the gauge section of the sample. The copper grips were held in place by grips that were tightened along the ends of the samples. Behind the grips were the cone jacks, which allowed for compressive stresses to be applied to the samples. The test setup can be seen in fig 25.

Chapter 5

Results and Discussion

5.1 Thermal expansion testing

After performing coefficient of thermal expansion tests and comparing the values as well as the error margin in the measurements, the values were calculated to be 12.22 ± 1.07 μm/m/°C for the 410SS and 13.60 ± 1.13 μm/m/°C for the mild steel as shown in 26. The study showed that even though there is a thermal expansion mismatch, the values are close enough to overlap and potentially indicate that shearing forces will not be sufficient to affect the dissimilar joint. Regarding thermal expansion mismatch, one thing to note is that the steels used in this system ultimately have martensite grains. According to Elmer et al., changes in composition that result in martensite or ferrite being present have the most significant effect on the CTE of a stainless steel weld [62]. Considering that the resulting microstructure throughout the entire system is martensitic, the thermal mismatch was expected to be low and negligible. The results, however, showed that although the error overlap shown indicates that the data may not have a statistically significant difference, it is not by any means conclusive.

Statistical analysis is needed to reach any concrete conclusions regarding thermal expansion mismatch. A p-test is performed to prove whether the difference is significant, and a p-value is obtained. In statistics, p is a statistical measure that helps determine whether a hypothesis is correct, or rather, it helps determine the significance of results. In this case, the hypothesis is that the difference in thermal expansion coefficients is not statistically significant. A t-test is first performed, which finds the value of the t statistic. The formula for this statistic is

$$t = \frac{\bar{x}_{410SS} - \bar{x}_{MS}}{\sqrt{\frac{(\sigma_{410SS})^2}{4} + \frac{(\sigma_{MS})^2}{4}}} \tag{5.1}$$

Where $\bar{x}_{410SS}$ and $\bar{x}_{MS}$ are the mean values of the 410SS and MS test results. (σ_{410SS} and σ_{MS} are the variances for both materials. This calculation yields a t value of 80.974. This value can be used to look up the corresponding p-values in a t-test table. This new value is compared to the 0.05 value, indicating if the difference in data is significant. The value obtained from the t-test table was 0.0005, which is significantly smaller than 0.05. This result means that there is a significant difference in the measured CTE data. The significance of this test is to determine whether the CTE mismatch will produce significant stresses on the material interface. Now that it is proven that this is indeed the case, the stresses on the interface must be quantified.

A thin-film analysis to determine whether the stresses are present at the interface is performed. For this case, 410SS is assumed to be the "thin-film" on the mild steel substrate. Work by Freund et al. shows that a film that is unbounded along the plane of the interface [63] has a relation such that

$$\sigma_0 = \frac{E}{1-\nu}\Delta T(\alpha_s - \alpha_f) \tag{5.2}$$

where E is Young's modulus, ΔT is the temperature change, ν is Poisson's of the film, and α_s and α_f are the coefficients of linear thermal expansion for the substrate and the film, respectively. After inputting the values, a stress value of 67 MPa is calculated. In chapter 3, there is a consideration regarding the stresses acting on the element previously shown. Now that the presence of thermal stresses has been proved and quantified, these can be considered and added to the stress element. The thermal stresses act in the same direction as σ_2 and σ_3, so these can be added. The stress element shown in fig 27 now shows a fully resolved system with thermal stresses due to CTE mismatch considered, and σ_1 and σ_2 now have a value of 202 MPa. It is highly likely that the stresses in the material interface caused potential plastic deformation that is discussed in the microscopy results.

5.2 Fatigue testing

Fatigue testing results show that plastic deformation occurs on all 4 samples as can be seen in figures 28,29,30 and 31. Something to note from the results is that during testing of samples 1 and 3, the CGauge used to measure diametral strain in the sample seems to have slipped, resulting in jumps in the plots and irregularities. Samples 2 and 4 showed no issues with the CGauge. An even more significant issue can be seen where sample 1 showed both compressive and tensile strains, whereas sample 2 shows only compressive strains. It seems likely that CGauge placement is a factor. However, the irregularity of the material interface makes it difficult to know what kind of deformation is to be expected at the location of the CGauge placement. The interface irregularity is likely due to the weld beads. The weld bead dimensions are shown in 5 where the weld bead dimensions can be seen to be over 2mm in both materials. Considering that the cross-sectional area of the sample is only around 10mm, one could see how easy it would be to place the CGauge in a different material in each of the tests, which seems to be so in this case. Testing was being done as consistently and carefully as possible by measuring the distance to the center of the gauge before each test.

According to the test results, it seems like samples 1 and 3 were measured on the mild steel side of the sample, seeing as the material showed both tensile and compressive strains, as well as large deformations. Samples 2 and 4 show only compressive strains and considerably less deformation, meaning that it is likely that the CGauge was placed on the 410SS, which was not expected to deform in the first place. There is no apparent change in stress amplitude in any of the samples, and it can also be seen in force-time plots. Force-time plots show consistent behavior throughout all four samples, as seen in figs 32, 33, 34, and 35.

The most significant difference is that in samples 1 and 3, the samples accumulated plastic deformation to the extent that significant tensile strain had to be applied for the system to return to the zero stroke position. Samples 2 and 4 showed no such behavior, as shown in the curves, where they were only exposed to compressive plastic deformation. This behavior is typical of ratcheting phenomena. Ratcheting occurs when a material is subjected to asymmetric cyclic loading, which was the case for this study as the test was designed only to apply compressive mechanical loading. It is an accumulation of plastic strain along the loading direction over time as shown by Paul et al. [64]. A literary stuyd written by Dahlberg et al. alsho show the same behavior describing it as ratcheting, where plastic deformation accumulates over time [65]. One thing that is consistent in all samples is that they all show signs of stress relaxation. This means that while the stress amplitude did not change, the mean stress and strain did change. Initial mean stress was measured at around 60 MPa, while the final mean stress seemed to be 0 MPa in all samples.

Something of note is that the cooling was not fast enough to keep up with the programmed temperature profile during testing. This phenomenon can be seen in figs. 36, 37, 38 and 39. It is possible that this discrepancy between the experimental and the programmed temperature caused the tempering response to be different from the predicted response, but the effects are currently not known. Indeed, this is an exciting subject to pursue beyond the scope of this work.

5.3 Microscopy

Fig. 40 shows the comparison of the as-printed microstructure and the heat-treated microstructure. In these images, the 410SS is located on the left side, and the mild steel is located on the right side. In the 410SS, untempered martensite and delta ferrite can be observed in fig. 41. With this, significant heterogeneity can be observed in the as-printed sample, where the solidified melt pools can be observed throughout the sample. The heat-treated sample shows great improvement in homogenizing the microstructure.

Interesting features were observed in all four fatigue-tested samples around the interface area. Figs 42,43,44 and 45 show large martensite laths that seem to be oriented at about 45 degrees. As the samples were cut to observe the gauge section throughout their axes, one can say that the uniaxial loading was done in the left and right direction of the images. Therefore, the 45 degrees can be assumed to be from the loading direction during testing.

Dieter shows that at 45 degrees from the uniaxial loading direction, the maximum shear stress is found. This finding could indicate that the microstructure could have gone through plastic deformation in the form of shear. The thermal stresses previously calculated are likely to have caused this deformation.

5.4 Hardness testing

Hardness testing shows significant scatter throughout the as-printed sample, as seen in fig. 46. In the as-printed condition, hardness values of 375 HV up to 440 HV can be observed in the 410SS side of the sample, while the mild steel region shows hardness values around 175 HV. After heat treatment, the material certainly shows more homogeneity, as seen in fig. 47. Hardness values were as high as 375 HV in some regions in the 410SS, while most of the 410SS showed 315 HV. This change in hardness is a potential reduction of around 16%. The mild steel shows hardness values around 200 HV after heat treatment for at least a 14% hardness increase. This increase is due to the as-printed microstructure being ferrite and the heat-treated microstructure being martensite, resulting in a hardness increase. The distribution of hardness in the as-printed and heat-treated condition is shown in fig.48. Despite heat treatment reducing heterogeneity in hardness, sharp hardness gradients are still present. The sites that show these hardness gradients can still present a challenge by becoming plastic deformation sites.

Observing the samples after fatigue testing shows that overall hardness was reduced, but something of note is that the sharp hardness gradients were not observed post-testing, as shown in fig. 49. A histogram for the hardness of the fatigue-tested samples is shown in fig. 50 where it can be observed that the hardness gradient is reduced and a normal distribution curve is observed as well. 410SS shows hardness values from 320 HV to 250 HV in most of the 410SS region, while the mild steel shows values at around 200 HV. 410SS values compare relatively well to the approximation done before testing where a hardness value of 303 was predicted using the Hollomon-Jaffe parameter on fig. 12. Compared to the resulting 315 HV value, this value shows a 4% difference from the hypothesized value but is still within the range of the actual values recorded.

The hardness values obtained after fatigue testing are compared to the temper response plots shown in fig. 11. A predicted hardness of 296 HV on the 410 at 600°C is within the range of the resulting hardness in most of the 410SS. Hardness values of 270 and 290 are observed in samples 1 and 3, respectively, but only at the left edge of the sample. Sample 1 shows lower hardness than the hypothesized value, but sample 3 compares well. Towards the interface, the values reduce to around 250 HV, lower than the hypothesized values. Sample 4 shows higher hardness than the other samples at 310 HV but reduces to 250 in the center of the 410SS region. Sample 2 showed a hardness value around 270 HV which is also lower than the predicted value of 296 HV. Overall, the samples showed lower hardness than the predicted values before fatigue testing. It must be mentioned that these predictions were done using curves for isothermal thermal loads and not the cyclic loads present during the test. Even so, this shows that the predicted values were higher than the actual test values even though the samples were never exposed to an isothermal load of 600°C. Overall, the hypothesized values do not vary significantly from the actual results, as most predicted hardness values were within the range of the test results.

The results show that, as expected, the materials went through plastic deformation over time, especially the mild steel due to ratcheting behavior. Plastic deformation was expected because the mild steel was exposed to loads beyond its predicted yield strength of 110 MPa since the beginning of fatigue testing. The four samples were exposed to a compressive stress of 65 MPa during the fatigue tests. According to these results, the dissimilar material system consisting of 410SS and mild steel might not meet the 42 HV hardness requirements for hot stamping applications with the deposition and heat treatments procedures used in this study. This subject merits further research to optimize the material system's properties by processing in various ways, such as the build parameters for deposition, heat treatment parameters, and surface improvement to make the system suitable for service. 410SS is a material commonly used in tooling applications, so optimizing its production parameters seems like an appropriate solution to improve its properties to the desired output.

The fatigue tests show that the heat treatment used to prepare the material for testing is not enough to meet service requirements, at least in mild steel. The 410SS seems to withstand the loading conditions, but the mild steel did not, as shown in the calculations made in chapter 3 on the loading conditions in the hot stamp. This does not mean that mild steel cannot be used for this application. Because these parts are additively manufactured, the geometry of the stamps can be modified to prevent the stamp from deforming. The hot stamp may not necessarily have to be produced with the 410SS just making up the outer casing. 410SS support structures can be produced relatively easily to provide a more rigid structure, while the mild steel can make up the cooling channels in the stamp.

One potential study area for this similar steel system is to investigate case hardening to improve surface properties that would make the system suitable for hot stamping applications. In 2021, Roy et al. published a study on the effects of shielding gas mixture on 410SS deposition to improve hardness and tensile strength [57]. The study showed that it is possible to obtain hardness values up to 424 ±10 HV and tensile strength of 1340 ± 34 MPa using an Argon with 3% N_2 mixture. These potential changes can effectively contribute to meeting the 42 HRC hardness criteria needed for hot stamping service. This study can be used to pursue similar work involving WAAM parts consisting of both 410SS and mild steel.

Post-test results show that the steep hardness gradients observed in the pre-test hardness map shown in figs. 46 and 47 were eliminated due to the extended time that the materials were exposed to high temperatures. The fatigue-tested samples plot shows how hardness gradually decreases. This is due to long-term tempering in the steels. As previously mentioned, this certainly merits an investigation into proper heat treatments designed for a dissimilar steel system with 410SS and mild steel. The heat treatment used in this study was initially designed for the 410SS only to eliminate hardness scatter with the elimination of δ-ferrite in the as-deposited 410SS. The results indicate that it could be possible to develop a heat treatment that effectively eliminates the steep hardness gradients that would eliminate sites for potential failure.

An improvement that can be made in future dissimilar sample preparation for fatigue testing or any testing involving taking measurements at the material interface is recommended. After machining the samples, a simple 4% nital etchant can be used on the surface to reveal the ferrite grains in the mild steel and the interface. This practice can significantly help increase consistency in CGauge placement. The interface is roughly 4mm wide as shown in fig 24 with an electron dispersive spectroscopy map taken to observe Cr diffusion between the two materials. The CGauge contact area with the sample is around 2mm wide, making it possible to locate a suitable site for placement that will ensure strain measurements are appropriately taken at the material interface. Regarding the CGauge slipping during testing, it is possible to adjust the spring force, preventing the CGauge from potentially slipping from its intended location. This was not done during the tests out of concern in breaking the quartz rod that serves as the contact point between the CGauge and the sample surface, as this would have meant significant delays in testing.

Chapter 6

Summary and Conclusion

6.1 Summary

1. Thermal expansion testing tests and data analysis showed that thermal expansion mismatch was present in the 410SS-MS interface as the thermal expansion coefficients show statistically significant variance with one another. Stress analysis was performed to quantify the thermal stresses at the interface to be 68 MPa, normal to the loading direction. These thermal stresses are possibly the reason that plastic deformation sites were observed along the interface.

2. Fatigue testing showed a significant stress relaxation behavior that led to plastic deformation in the samples at 0.12mm stroke, where the stress amplitude did not change. However, the mean stresses did change from 60 MPa to 0 MPa. Samples 1 and 3 showed erroneous strain measurements that were of little use. All four samples showed a reduction in force, indicating that the materials had become plastically deformed as the tests progressed. The behavior exhibited by samples 1 and 3 resembled that of ratcheting, where the accumulation of plastic deformation was observed.

3. Microscopy imaging showed that the materials were fully martensitic after tempering heat treatment. After fatigue testing, potential sites of plastic deformation were observed where very large martensite laths were oriented about 45 degrees from the direction of uniaxial loading. This conclusion is reached since maximum shear occurs

at 45 degrees from the loading direction in a cylindrical sample, as shown by Dieter. These microstructures strongly indicated evidence of plastic deformation in the form of shearing along the interface.

4. Hardness testing showed a reduction in hardness in the 410SS from 375 HV in the as-printed condition to 310 HV in the heat-treated condition and a further reduction to 250 HV after fatigue testing. Mild steel showed a hardness increase of 20% after heat treatment, from 175 HV to 200 HV. The hardness values were lower than the predicted values using the Hollomon-Jaffe. The predicted values were still within the range of the actual test results. Comparing results from different processing stages shows that the sharp hardness gradients observed in heat-treated samples are eliminated after fatigue testing. This elimination is potentially due to long-term high-temperature exposure allowing carbon atoms to diffuse out of BCT lattices in the martensite laths.

6.2 Conclusion

This study aimed to assess dissimilar steel fatigue performance. Another item that this study aimed to answer was how can dissimilar steel hot stamps fail during service. Based on quantitative studies, it can be concluded that dissimilar hot stamps can fail due to plastic deformation due to long-time cyclic high-temperature and mechanical loading. This failure can be observed in the reduction of yield strength, hardness, and force required to deform the die stamp materials. More importantly, this study showed that further material processing is required for the dissimilar materials to meet hot stamping application requirements. A significant contribution from this study is that it sets a baseline for further studies on 410 martensitic stainless steel and mild steel dissimilar systems as there is little work in the literature regarding this system.

Improvements in this study can be made to obtain more consistent results. One recommendation is to develop heat treatments designed for dissimilar steel materials. Another recommendation is to ensure better practices in taking measurements during testing, such as verifying that the material interface is well identified and visible by using etchants.

Bibliography

[1] Geogre E Dieter. Mechanical metallurgy, mc graw hill book. *New York (1988)*, 1986. ix, 4, 6, 14, 49

[2] J.R Davis. Selection of wrought martensitic stainless steels. *ASM Handbook, Volume 6: Welding, Brazing, and Soldering*, 6:432–442, 1993. ix, 6, 50

[3] Manuela Galati. Electron beam melting process: a general overview. *Additive Manufacturing*, pages 277–301, 2021. ix, 10, 51

[4] Eleonora Atzeni and Alessandro Salmi. Economics of additive manufacturing for end-usable metal parts. *The International Journal of Advanced Manufacturing Technology*, 62(9-12):1147–1155, 2012. ix, 11, 51

[5] Manfred Geiger, Marion Merklein, and Jürgen Lechler. Determination of tribological conditions within hot stamping. *Production Engineering*, 2(3):269, 2008. ix, 52

[6] K. Mori, P.F. Bariani, B.-A. Behrens, A. Brosius, S. Bruschi, T. Maeno, M. Merklein, and J. Yanagimoto. Hot stamping of ultra-high strength steel parts. *CIRP Annals*, 66(2):755–777, 2017. 1, 6

[7] M Merklein and J Lechler. Investigation of the thermo-mechanical properties of hot stamping steels. *Journal of materials processing technology*, 177(1-3):452–455, 2006. 1, 5

[8] Eric Michael Tenuta. *Material properties and mechanical behaviour of large-scale additively manufactured multi-layered steels*. PhD thesis, University of Ontario Institute of Technology (Canada), 2020. 1, 18

[9] Hossein Karbasian and A Erman Tekkaya. A review on hot stamping. *Journal of Materials Processing Technology*, 210(15):2103–2118, 2010. 2

[10] G Berglund. The history of hardening of boron steel in northern sweden. In *1st international conference on hot sheet metal forming of high-performance steel, Kassel, Germany*, volume 175, page 177, 2008. 2

[11] A Naganathan and L Penter. Hot stamping. *Sheet metal forming-processes and applications. Materials Park, OH: ASM International*, pages 133–42, 2012. 2, 4, 5, 6

[12] Malte Gebler, Anton JM Schoot Uiterkamp, and Cindy Visser. A global sustainability perspective on 3d printing technologies. *Energy Policy*, 74:158–167, 2014. 2, 10, 11

[13] Andrzej Nycz, Adeola I Adediran, Mark W Noakes, and Lonnie J Love. Large scale metal additive techniques review. In *Proceedings of the 27th Annual International Solid Freeform Fabrication Symposium*, 2016. 2, 9, 11, 12

[14] Helen Lockett, Jialuo Ding, Stewart Williams, and Filomeno Martina. Design for wire+ arc additive manufacture: design rules and build orientation selection. *Journal of Engineering Design*, 28(7-9):568–598, 2017. 2

[15] Sougata Roy, Benjamin Shassere, Jake Yoder, Andrzej Nycz, Mark Noakes, Badri K Narayanan, Luke Meyer, Jonathan Paul, and Niyanth Sridharan. Mitigating scatter in mechanical properties in aisi 410 fabricated via arc-based additive manufacturing process. *Materials*, 13(21):4855, 2020. 5, 21, 22

[16] AV Vlasov. Thermomechanical fatigue of dies for hot stamping. *Steel in Translation*, 46(5):356–360, 2016. 5, 6, 14

[17] Anna Medvedeva, Jens Bergström, Staffan Gunnarsson, and Jörgen Andersson. High-temperature properties and microstructural stability of hot-work tool steels. *Materials Science and Engineering: A*, 523(1-2):39–46, 2009. 5

[18] Gopa Chakraborty, CR Das, SK Albert, AK Bhaduri, V Thomas Paul, G Panneerselvam, and Arup Dasgupta. Study on tempering behaviour of aisi 410 stainless steel. *Materials Characterization*, 100:81–87, 2015. 5, 21

[19] S Ghadar, A Momeni, B Tolaminejad, and M Soltanalinezhad. A comparative study on the hot deformation behavior of 410 stainless and k100 tool steels. *Materials Science and Engineering: A*, 760:394–406, 2019. 5

[20] L. Briottet, J.J. Jonas, and F. Montheillet. A mechanical interpretation of the activation energy of high temperature deformation in two phase materials. *Acta Materialia*, 44(4):1665–1672, 1996. 5

[21] Donald R. Askeland. *Strain Hardening and Annealing*, pages 188–215. Springer US, Boston, MA, 1996. 6

[22] Katsuaki Kubota RyuichiroEbara. Failure analysis of hot forging dies for automotive components. *Engineering Failure Analysis*, 15:881–893, October 2008. 6

[23] Y Murakami and KJ Miller. What is fatigue damage? a view point from the observation of low cycle fatigue process. *International Journal of Fatigue*, 27(8):991–1005, 2005. 6

[24] B-A Behrens and F Schäfer. Service life predictions for hot bulk forming tools. *steel research international*, 80(12):887–891, 2009. 6

[25] GA Berti and M Monti. Thermo-mechanical fatigue life assessment of hot forging die steel. *Fatigue & fracture of engineering materials & structures*, 28(11):1025–1034, 2005. 6

[26] Nader Asnafi. Tool and die making, surface treatment, and repair by laser-based additive processes. *BHM Berg- und Hüttenmännische Monatshefte*, 166(5):225–236, 2021. 6

[27] Grant Ken-Hicken. Gas-Tungsten Arc Welding[1]. In *Welding, Brazing and Soldering*. ASM International, 01 1993. 7, 21

[28] John O Milewski. Additive manufacturing of metals. *Cham: Springer International Publishing*, 2017. 7

[29] JA Manriquez-Frayre and DL Bourell. Selective laser sintering of binary metallic powder. In *1990 International Solid Freeform Fabrication Symposium*, 1990. 7

[30] William J Sames, FA List, Sreekanth Pannala, Ryan R Dehoff, and Sudarsanam Suresh Babu. The metallurgy and processing science of metal additive manufacturing. *International materials reviews*, 61(5):315–360, 2016. 8, 10

[31] Lourdes D Bobbio, Richard A Otis, John Paul Borgonia, R Peter Dillon, Andrew A Shapiro, Zi-Kui Liu, and Allison M Beese. Additive manufacturing of a functionally graded material from ti-6al-4v to invar: Experimental characterization and thermodynamic calculations. *Acta Materialia*, 127:133–142, 2017. 8

[32] PL Blackwell. The mechanical and microstructural characteristics of laser-deposited in718. *Journal of materials processing technology*, 170(1-2):240–246, 2005. 8

[33] Heinz Steinbeiss, Hyunwoo So, Thomas Michelitsch, and Hartmut Hoffmann. Method for optimizing the cooling design of hot stamping tools. *Production Engineering*, 1(2):149–155, 2007. 8

[34] MM Gharbi. Innovative die technology—a paradigm shift for an efficient solution. In *Advanced High Strength Steel and Press Hardening: Proceedings of the 4th International Conference on Advanced High Strength Steel and Press Hardening (ICHSU2018)*, pages 421–430. World Scientific, 2019. 8

[35] R Muvunzi, D Hagedorn-Hansen, S Matope, X Madyibi, CB Swart, and M Nagel. Industry case study: process chain for manufacturing of a large hybrid hot stamping tool with conformal cooling channels. *The International Journal of Advanced Manufacturing Technology*, 110(7):1723–1730, 2020. 9

[36] Tarasankar DebRoy, HL Wei, JS Zuback, T Mukherjee, JW Elmer, JO Milewski, Allison Michelle Beese, AD Wilson-Heid, A De, and W Zhang. Additive manufacturing of metallic components–process, structure and properties. *Progress in Materials Science*, 92:112–224, 2018. 10

[37] Bhaskar Dutta, Sudarsanam Babu, and Bradley H Jared. *Science, technology and applications of metals in additive manufacturing*. Elsevier, 2019. 11

[38] David Whittaker and Francis H Sam Froes. Future prospects for titanium powder metallurgy markets. In *Titanium powder metallurgy*, pages 579–600. Elsevier, 2015. 11

[39] C Lindemann, U Jahnke, M Moi, and R Koch. Impact and influence factors of additive manufacturing on product lifecycle costs. In *Proceedings of the 24th Solid Freeform*

Fabrication Symposium, pages 998–1009. Sffsymposium Texas University Paderborn, Germany, 2013. 11

[40] Douglas S Thomas, Stanley W Gilbert, et al. Costs and cost effectiveness of additive manufacturing. *NIST special publication*, 1176:12, 2014. 12

[41] Chris Holshouser, Clint Newell, Sid Palas, Lonnie J Love, Vlastimil Kunc, Randall F Lind, Peter D Lloyd, John C Rowe, Craig A Blue, Chad E Duty, et al. Out of bounds additive manufacturing. *Advanced Materials and Processes*, 171(3), 2013. 12

[42] CR Cunningham, Sondre Wikshåland, Fangda Xu, Nneji Kemakolam, A Shokrani, Vimal Dhokia, and ST Newman. Cost modelling and sensitivity analysis of wire and arc additive manufacturing. *Procedia Manufacturing*, 11:650–657, 2017. 12

[43] JD Farren, JN DuPont, and FF Noecker. Fabrication of a carbon steel-to-stainless steel transition joint using direct laser deposition-a feasibility study. *WELDING JOURNAL-NEW YORK-*, 86(3):55, 2007. 13

[44] CD Lundin. Dissimilar metal welds-transition joints literature review. *Welding Journal*, 61(2):58–63, 1982. 13

[45] N.E. Dowling. *Mechanical Behavior of Materials: Engineering Methods for Deformation, Fracture, and Fatigue*. Prentice Hall, 1993. 13

[46] A. Niino M. and, Suzuki, T. Hirai, R. Watanabe, T. Hirano, and N Kuroishi. Method of producing a functionally gradient material. U.S. Patent No. 4,751,099, June 1988. 15

[47] Pierre Muller, Pascal Mognol, and Jean-Yves Hascoet. Modeling and control of a direct laser powder deposition process for functionally graded materials (fgm) parts manufacturing. *Journal of Materials Processing Technology*, 213(5):685–692, 2013. 15

[48] E. Tenuta, A. Nycz, M. Noakes, S. Simunovic, and M.H.A. Piro. Material properties and mechanical behaviour of functionally graded steel produced by wire-arc additive manufacturing. *Additive Manufacturing*, 46, 2021. 15, 18

[49] Takuya Kusunoki. *Quantification of the Tempering Response in Type 410 Steel Welds.* PhD thesis, The Ohio State University, 2020. 19

[50] David Tabor. *The hardness of metals.* Oxford university press, 2000. 20

[51] Ju Chen, Ben Young, and Brian Uy. Behavior of high strength structural steel at elevated temperatures. *Journal of structural engineering*, 132(12):1948–1954, 2006. 20

[52] D.H Mesa, A Toro, A Sinatora, and A.P Tschiptschin. The effect of testing temperature on corrosion–erosion resistance of martensitic stainless steels. *Wear*, 255(1):139–145, 2003. 14th International Conference on Wear of Materials. 21

[53] M.C. Tsai, C.S. Chiou, J.S. Du, and J.R. Yang. Phase transformation in aisi 410 stainless steel. *Materials Science and Engineering: A*, 332(1):1–10, 2002. 21

[54] L Schäfer. Influence of delta ferrite and dendritic carbides on the impact and tensile properties of a martensitic chromium steel. *Journal of Nuclear Materials*, 258-263:1336–1339, 1998. 21

[55] Niyanth Sridharan and Kevin Field. A road map for the advanced manufacturing of ferritic-martensitic steels. *Fusion Science and Technology*, 75(4):264–274, 2019. 21

[56] David J Stone, Boian T Alexandrov, and Jorge A Penso. Control of retained delta ferrite in type 410 stainless steel. In *Pressure Vessels and Piping Conference*, volume 57991. American Society of Mechanical Engineers, 2017. 21

[57] Sougata Roy, Bishal Silwal, Andrzej Nycz, Mark Noakes, Ercan Cakmak, Peeyush Nandwana, and Yukinori Yamamoto. Investigating the effect of different shielding gas mixtures on microstructure and mechanical properties of 410 stainless steel fabricated via large scale additive manufacturing. *Additive Manufacturing*, 38:101821, 2021. 22, 35

[58] A. Bahrami, S.H. Mousavi Anijdan, M.A. Golozar, M. Shamanian, and N. Varahram. Effects of conventional heat treatment on wear resistance of aisi h13 tool steel. *Wear*, 258(5):846–851, 2005. 22

[59] Anna Ermakova, Ali Mehmanparast, Supriyo Ganguly, Javad Razavi, and Filippo Berto. Investigation of mechanical and fracture properties of wire and arc additively manufactured low carbon steel components. *Theoretical and Applied Fracture Mechanics*, 109:102685, 2020. 22, 23

[60] George F Vander Voort, Steven R Lampman, Bonnie R Sanders, Gayle J Anton, Carol Polakowski, Jill Kinson, Kathryn Muldoon, Scott D Henry, and William W Scott Jr. Asm handbook. *Metallography and microstructures*, 9, 2004. 24

[61] Dynamic Systems Inc. *Gleeble Users Training Manual*, 2013. 27

[62] JW Elmer, DL Olson, and DK Matlock. Thermal expansion characteristics of stainless steel weld metal. *WELDING J.*, 61(9):293, 1982. 29

[63] LB Freund and Y Hu. Shear stress at a film-substrate interface due to mismatch strain. Technical report, Brown Univ Providence RI Div of Engineering, 1988. 30

[64] Surajit Kumar Paul. A critical review of experimental aspects in ratcheting fatigue: microstructure to specimen to component. *Journal of Materials Research and Technology*, 8(5):4894–4914, 2019. 32

[65] M Dahlberg and P Segle. Evaluation of models for cyclic plastic deformation–a literature study. *Swedish Radiation Safety Authority SMM*, 2010. 32

Appendices

A Figures

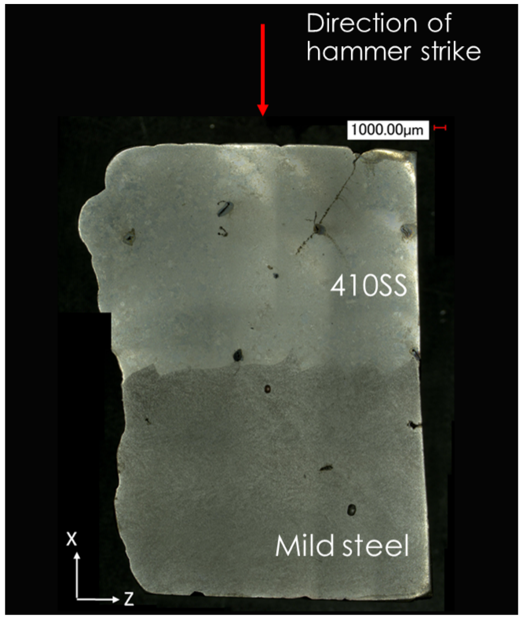

Figure 1: Sample used for hammer experiment.

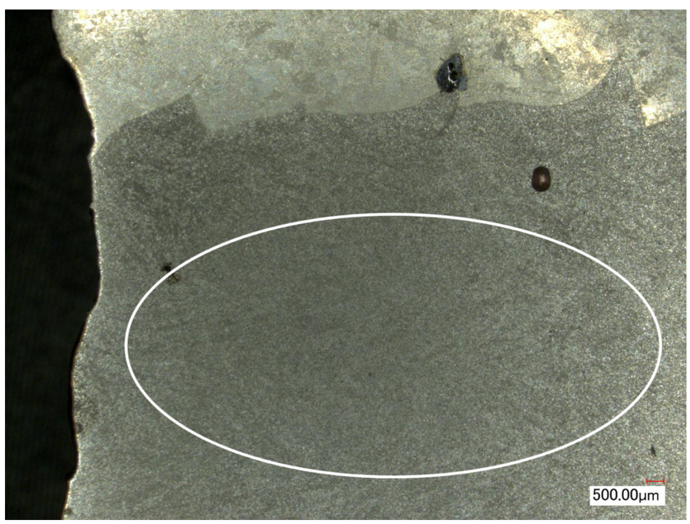

Figure 2: Patterns indicating possible flow lines after being struck with hammer.

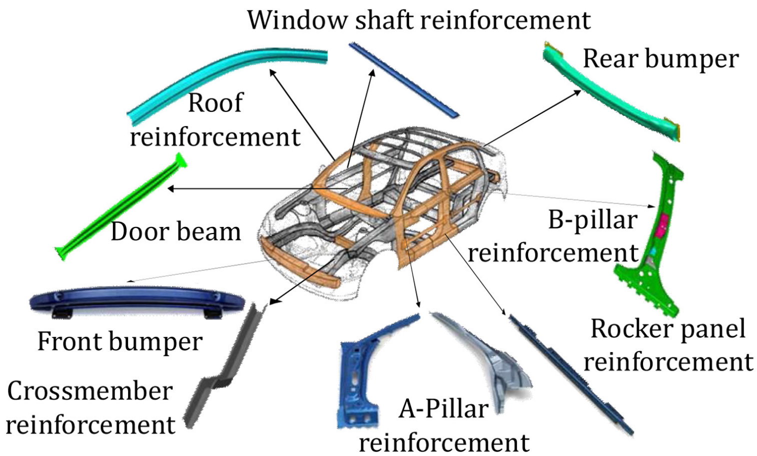

Figure 3: Different parts geometries made via hot stamping for automotive applications

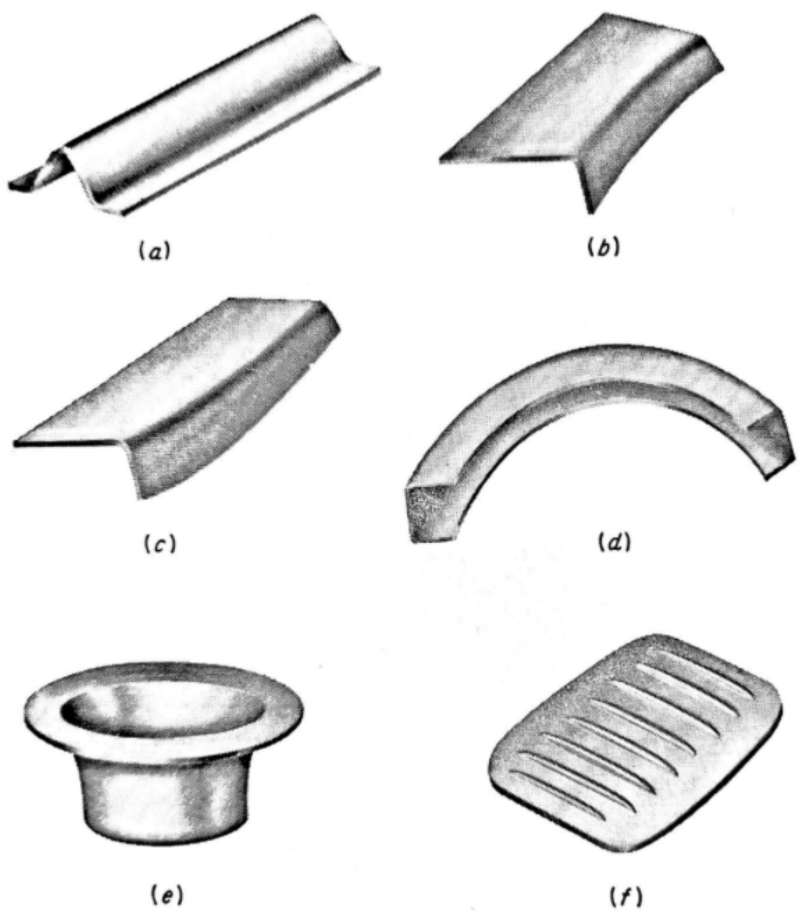

Figure 4: Typical formed shapes in hot stamping. a) Singly curved; b) stretch flange; c) shrink flange; d) curved sections; 3) deep-drawn cup; f) beaded section [1]

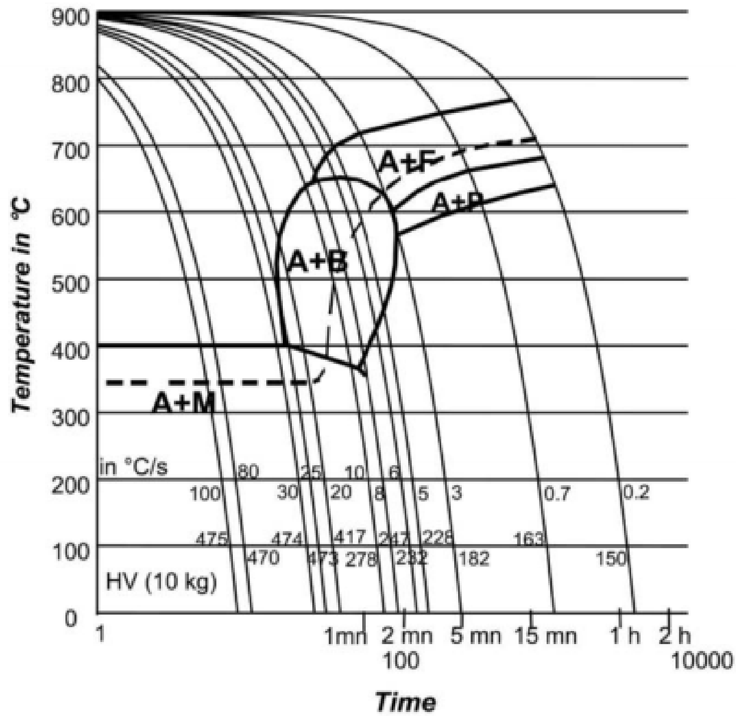

Figure 5: Time-Temperature-Transformation diagram for 25Mn5B boron steel [2]

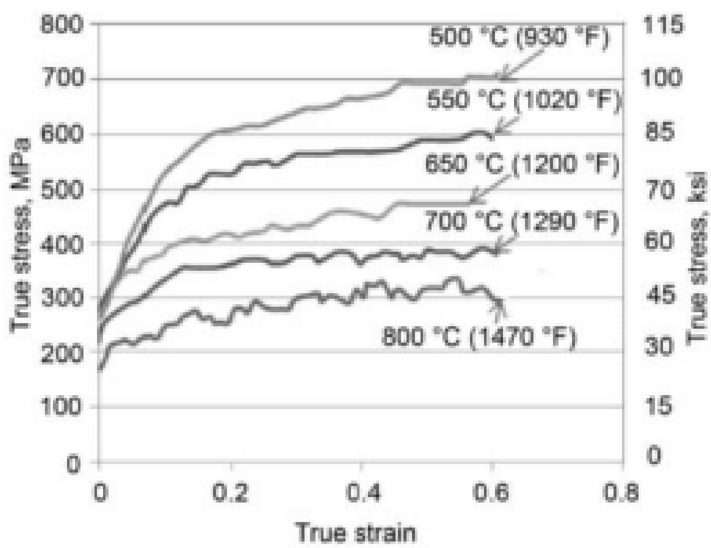

Figure 6: Temperature-dependent flow curves for 22MnB5 boron steel [2]

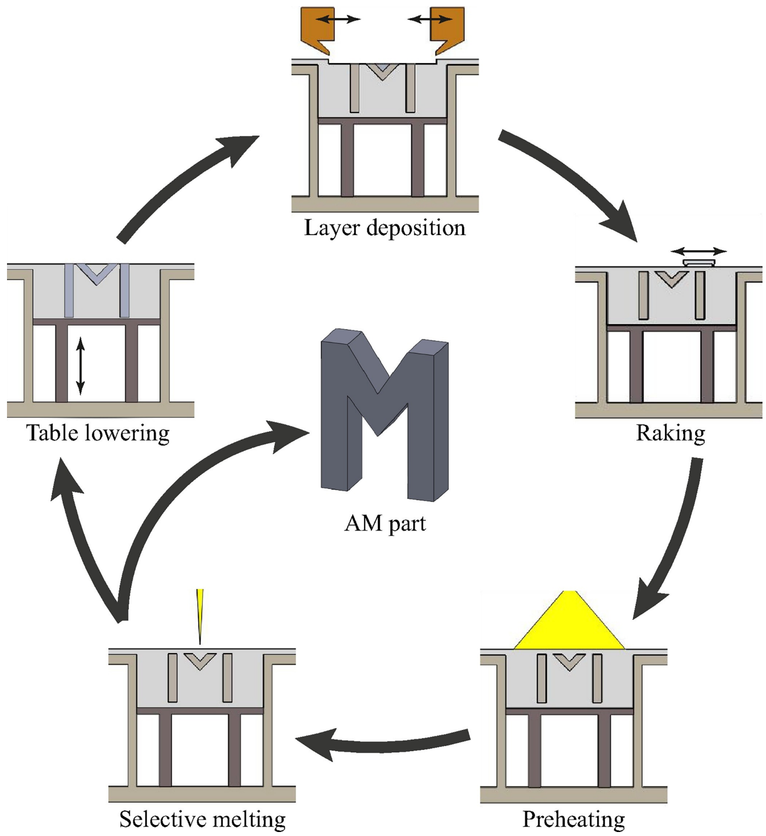

Figure 7: Powder-bed deposition cycle [3]

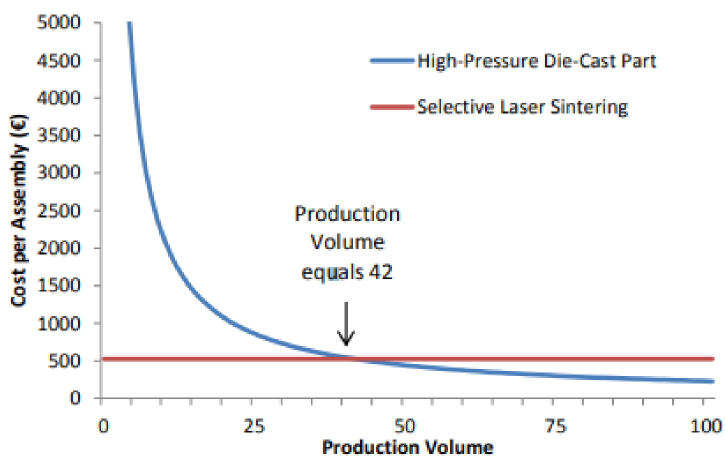

Figure 8: Break even point for High-Pressure Die Casting and Selective Laser Sintering [4]

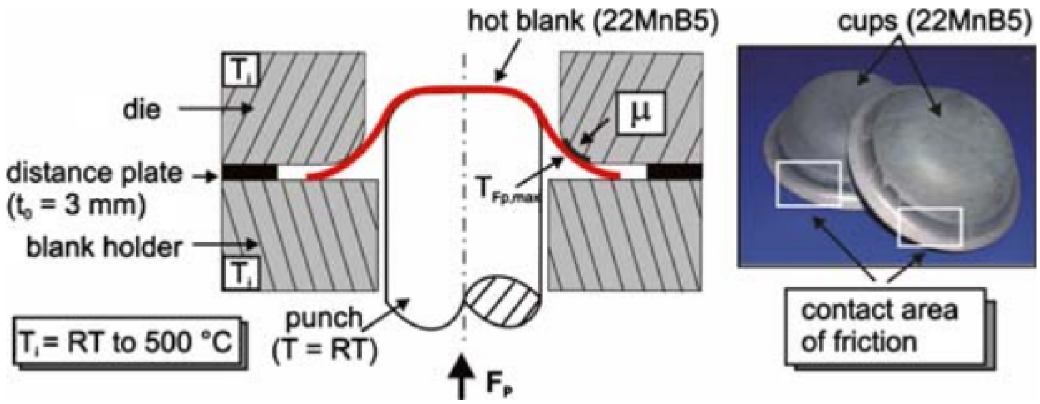

Figure 9: Contact surfaces between stamp and worksheet [5]

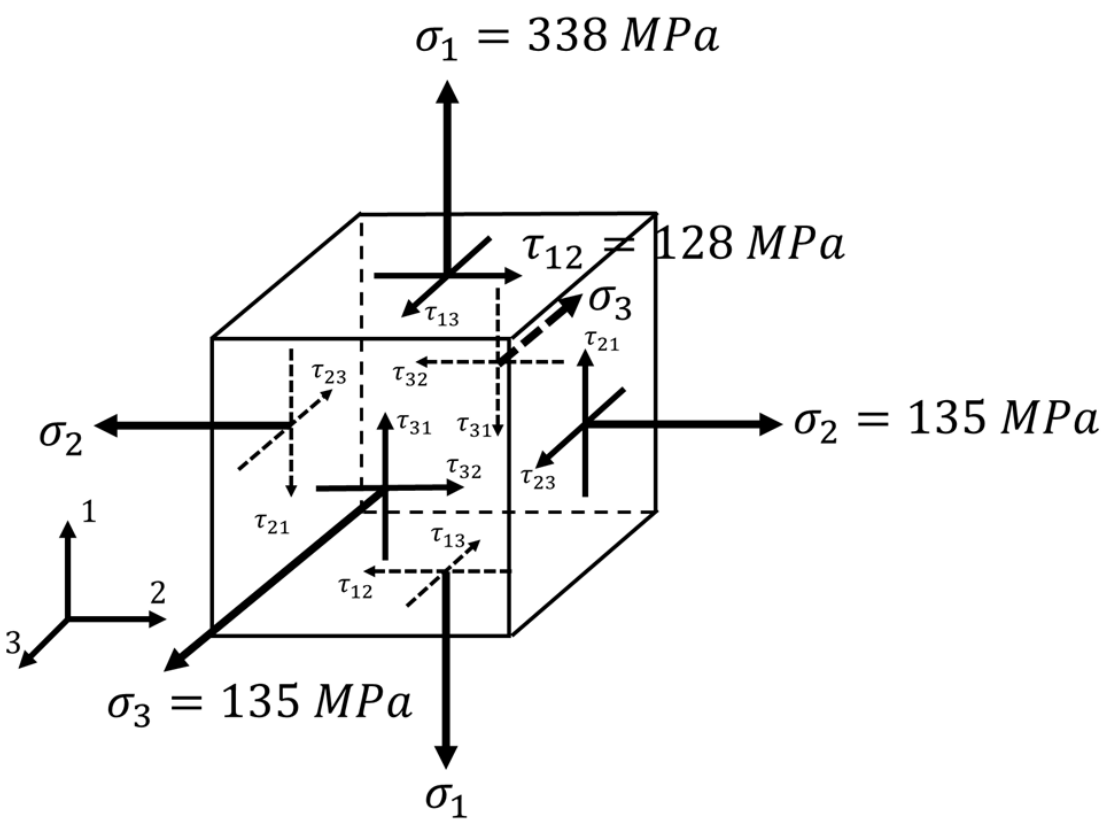

Figure 10: Stress element on surface of the die stamp

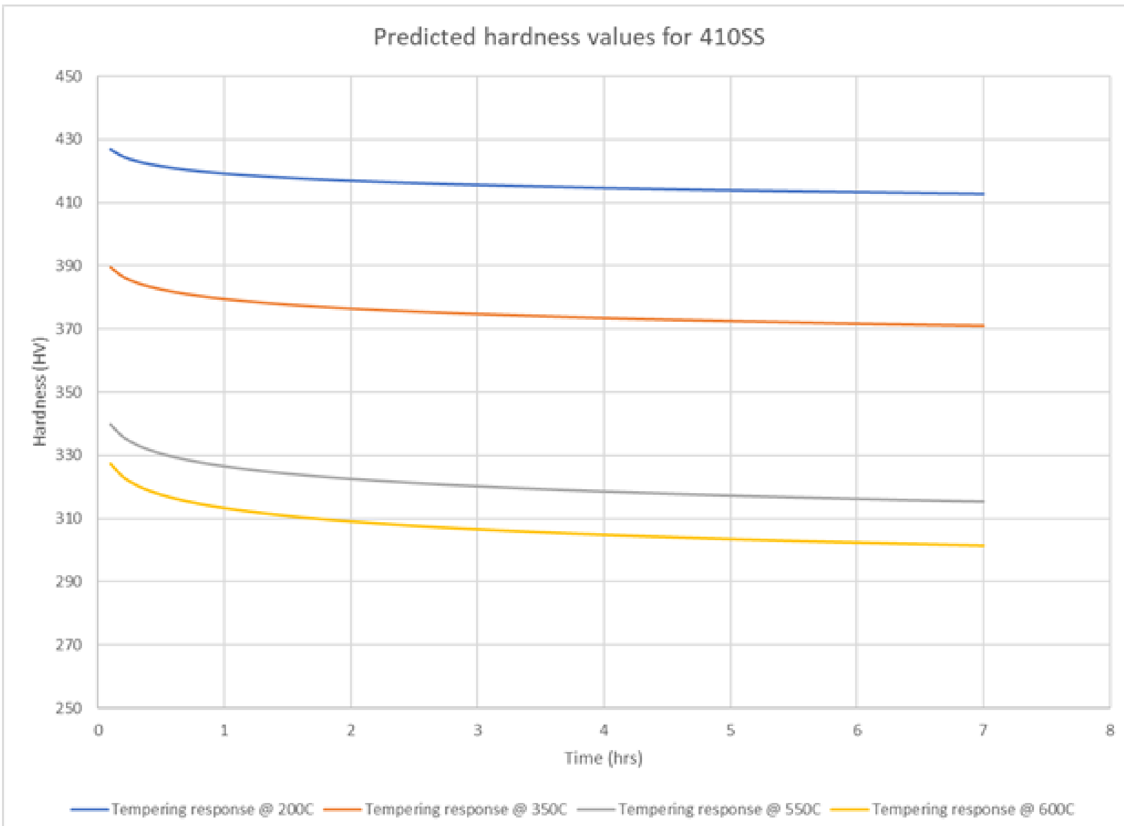

Figure 11: 410 SS predicted hardness values over time in four temperature ranges

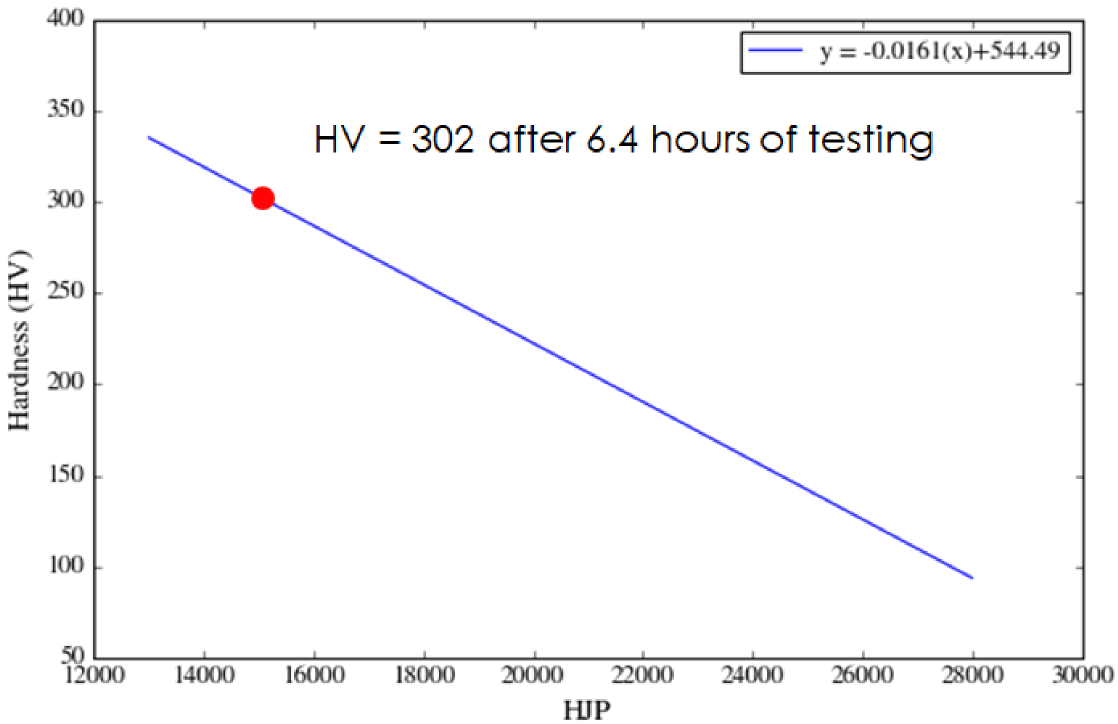

Figure 12: 410 SS predicted hardness values for 6.4 hours at 600°C

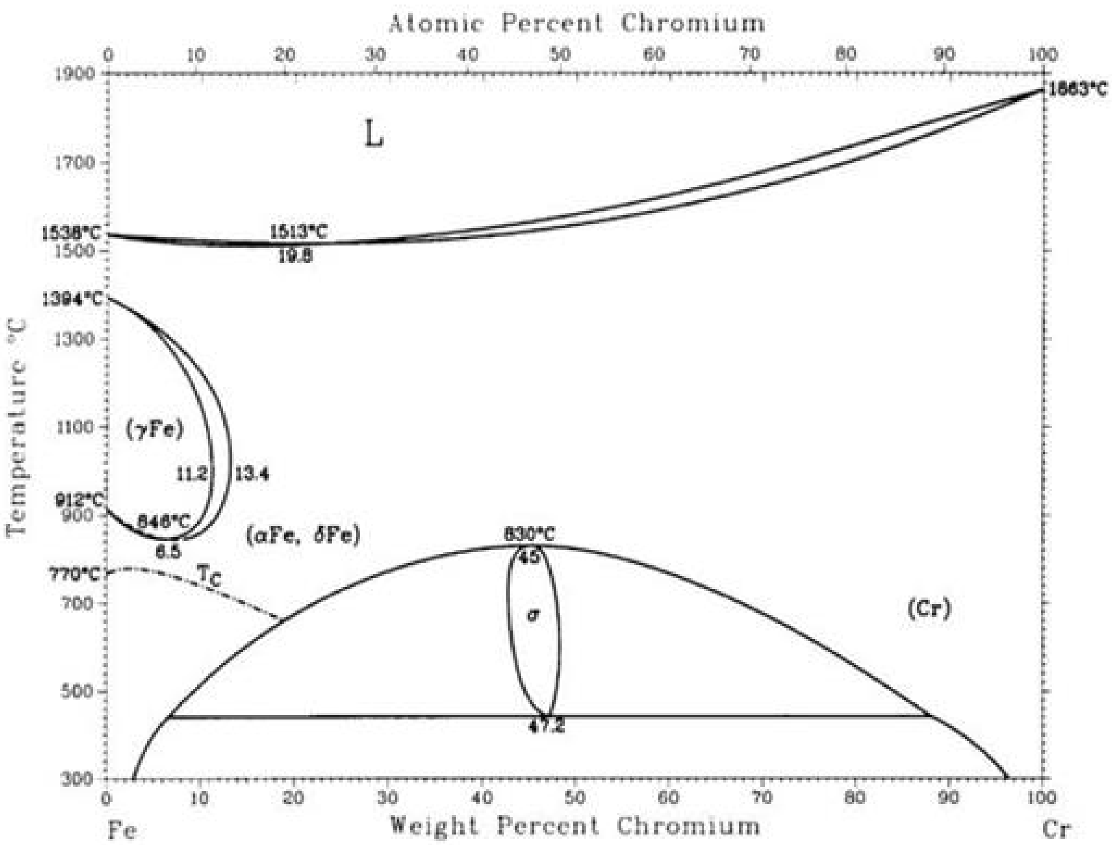

Figure 13: Iron-Chromium system phase diagram

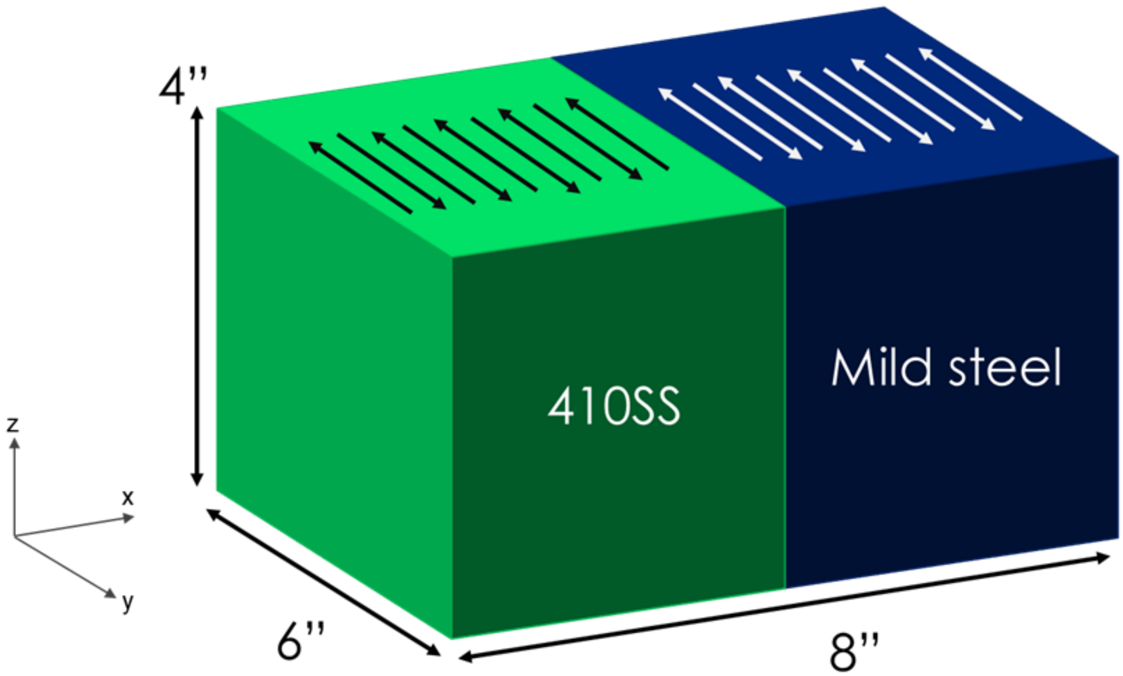

Figure 14: WAAM part used in this study

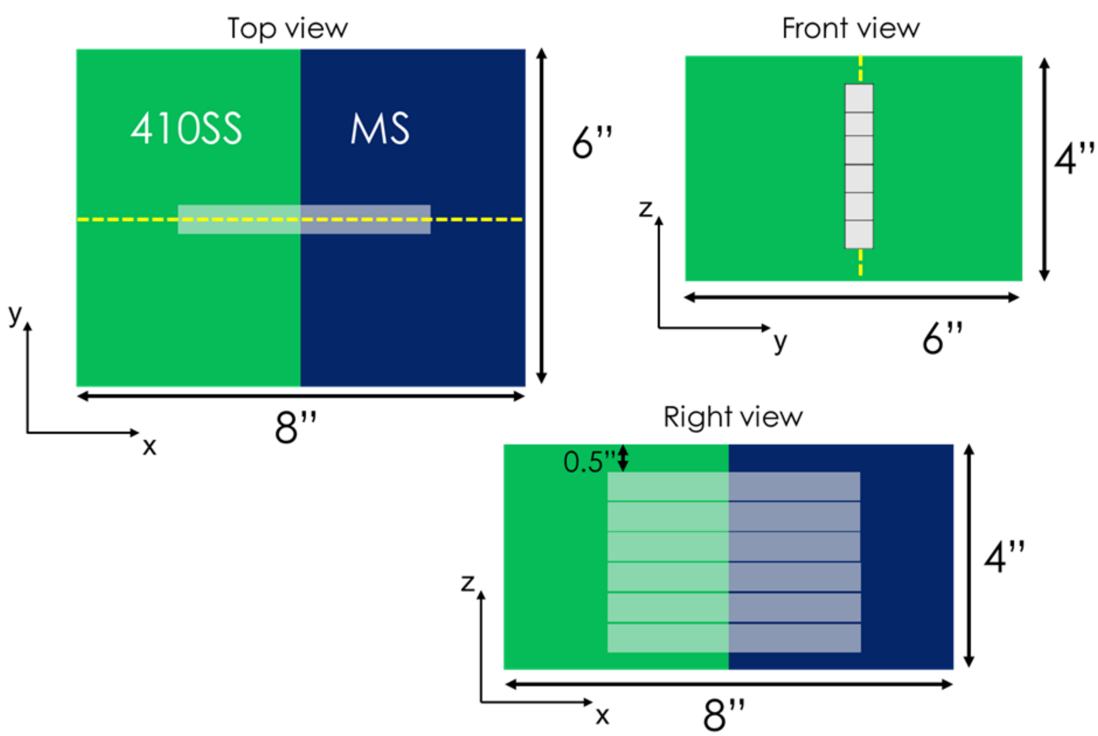

Figure 15: WAAM part dimensions

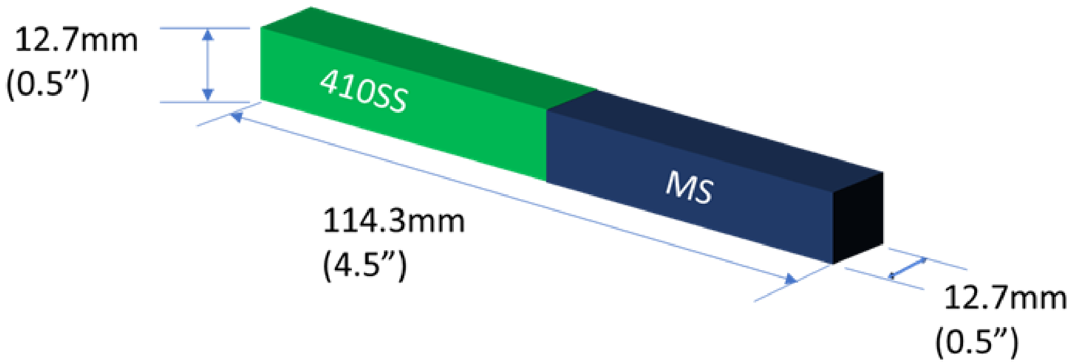

Figure 16: Dimensions for sectioned bars

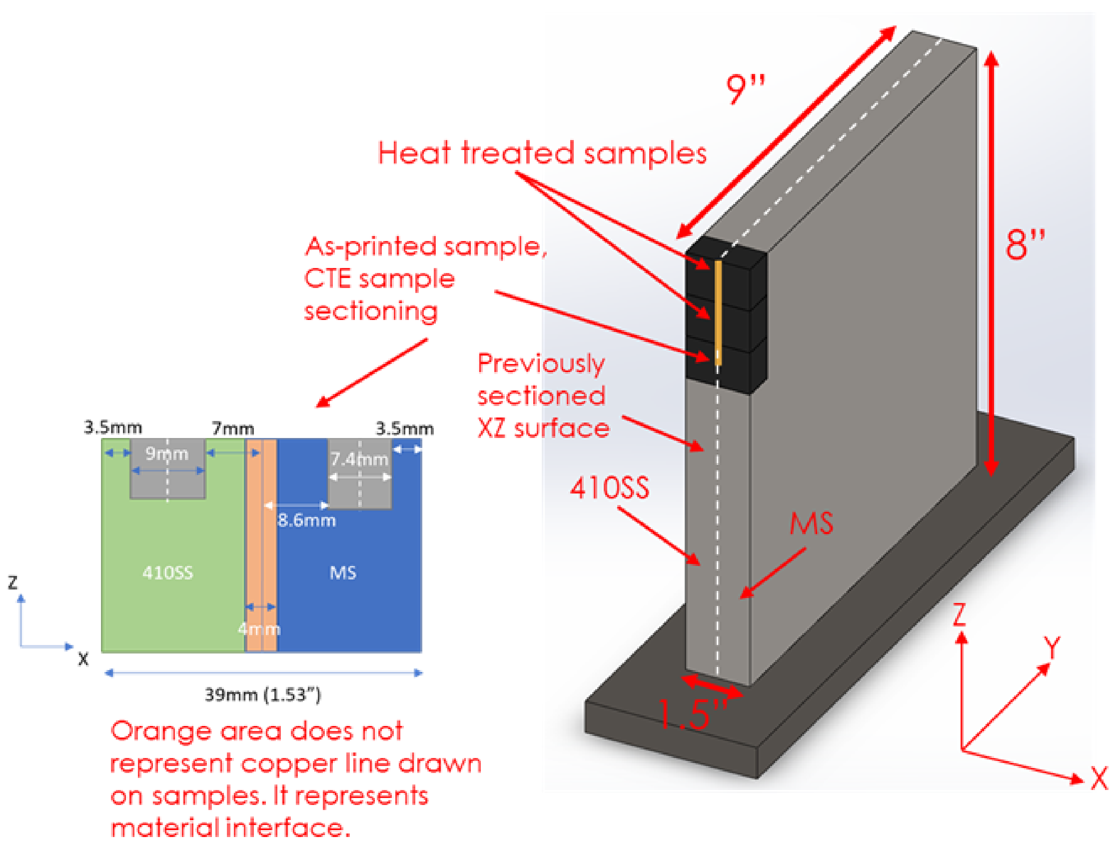

Figure 17: Sample schematic for thermal expansion testing

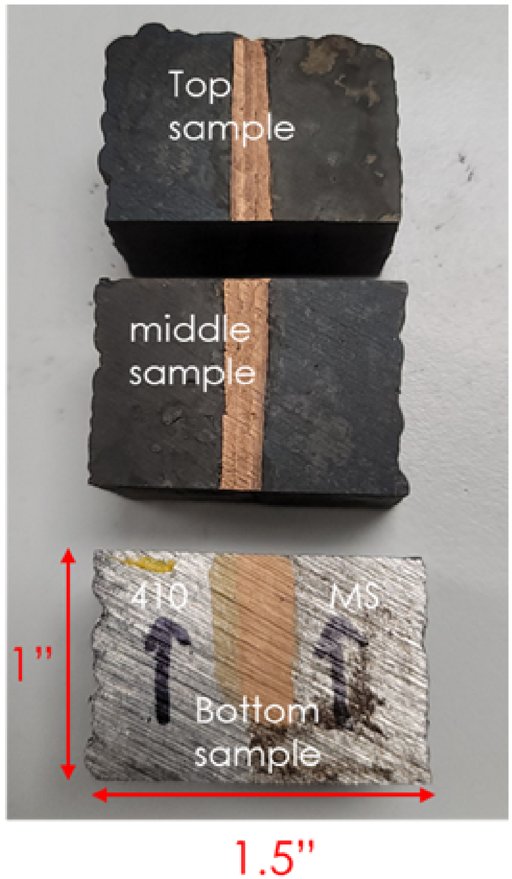

Figure 18: Samples sectioned from wall

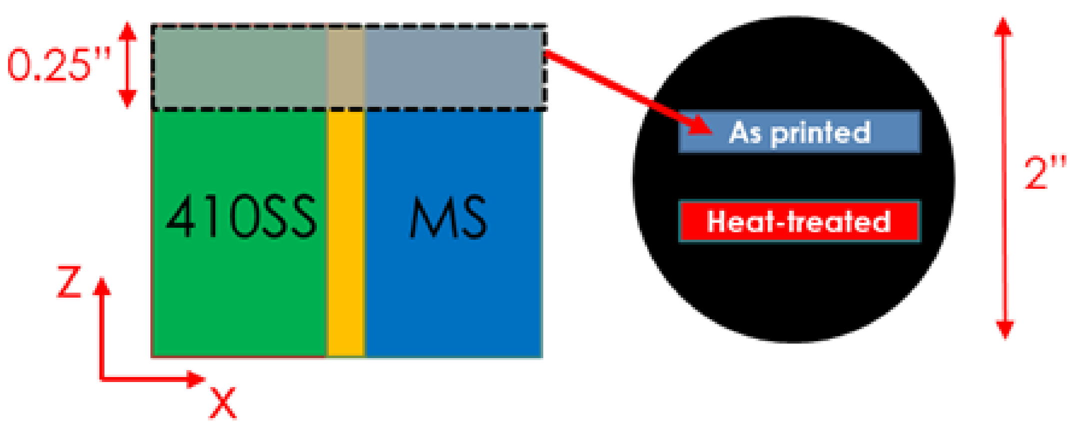

Figure 19: Sample schematic for optical microscopy and hardness testing

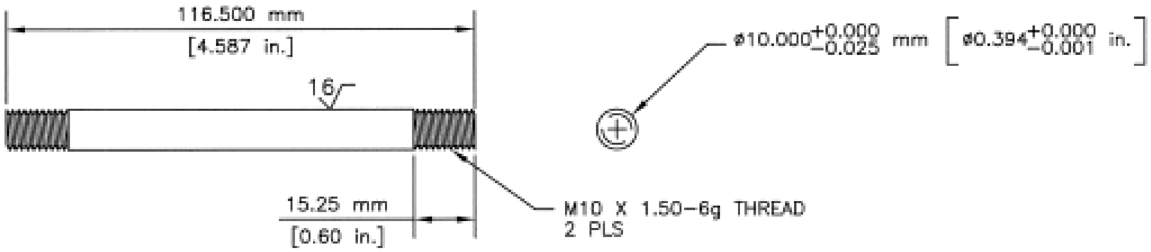

Figure 20: Samples dimensions used for fatigue testing

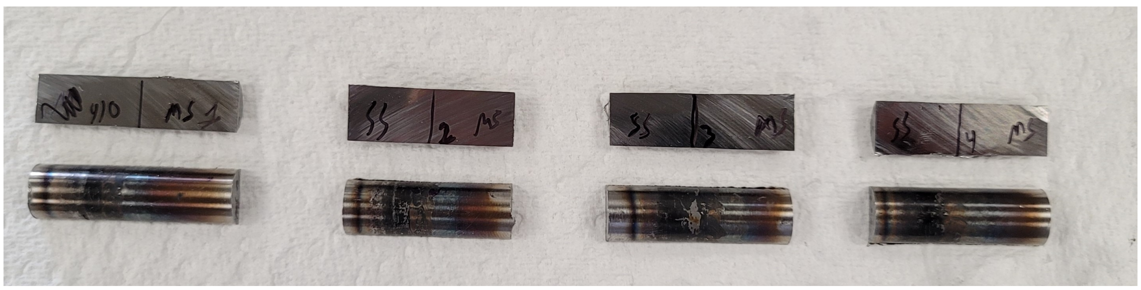

Figure 21: Sectioned gleeble samples after testing

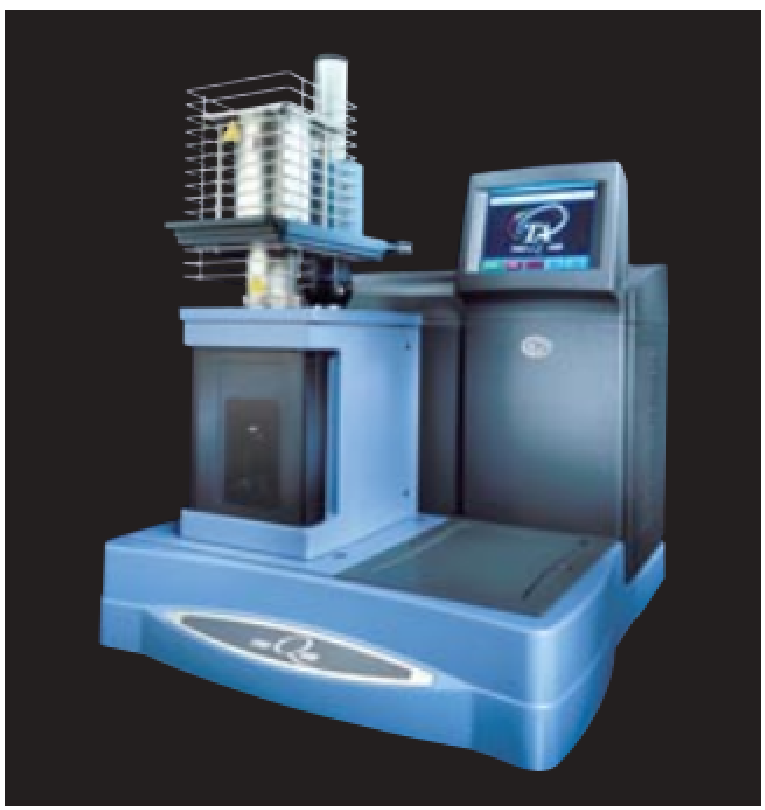

Figure 22: TA Q400 thermomechanical analizer

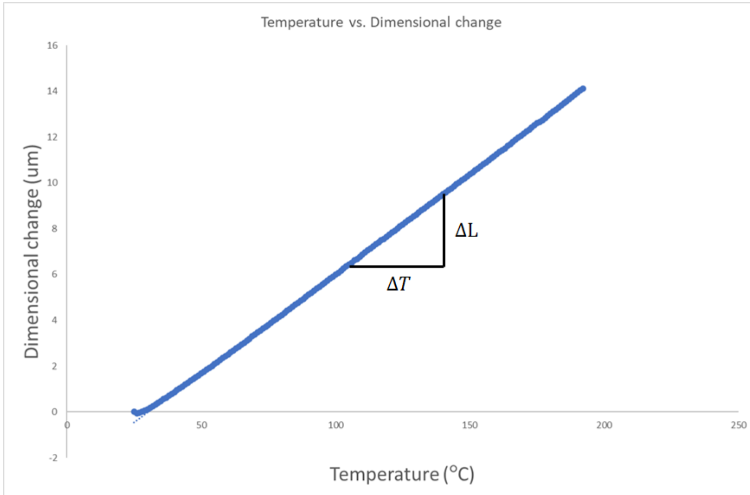

Figure 23: Raw CTE data showing plot of dimensional change as a function of temperature

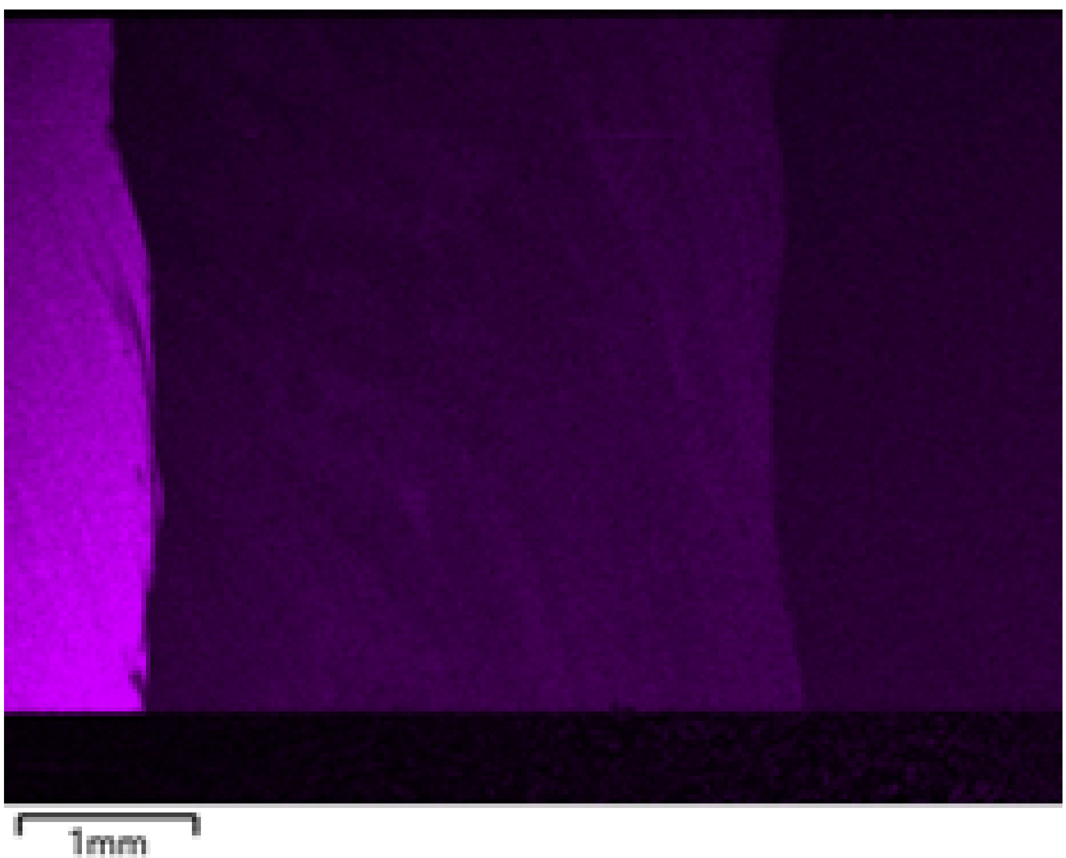

Figure 24: Cr mapping along dissimilar sample interface

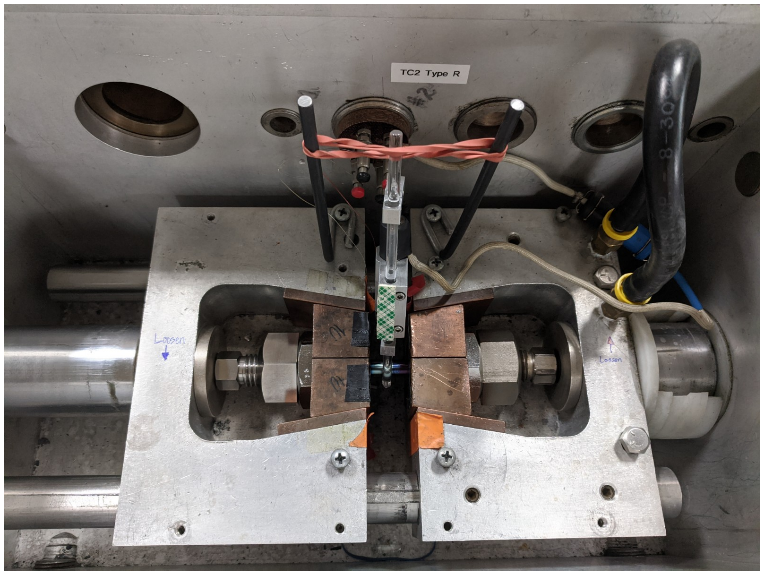

Figure 25: Test setup in the Gleeble 1500

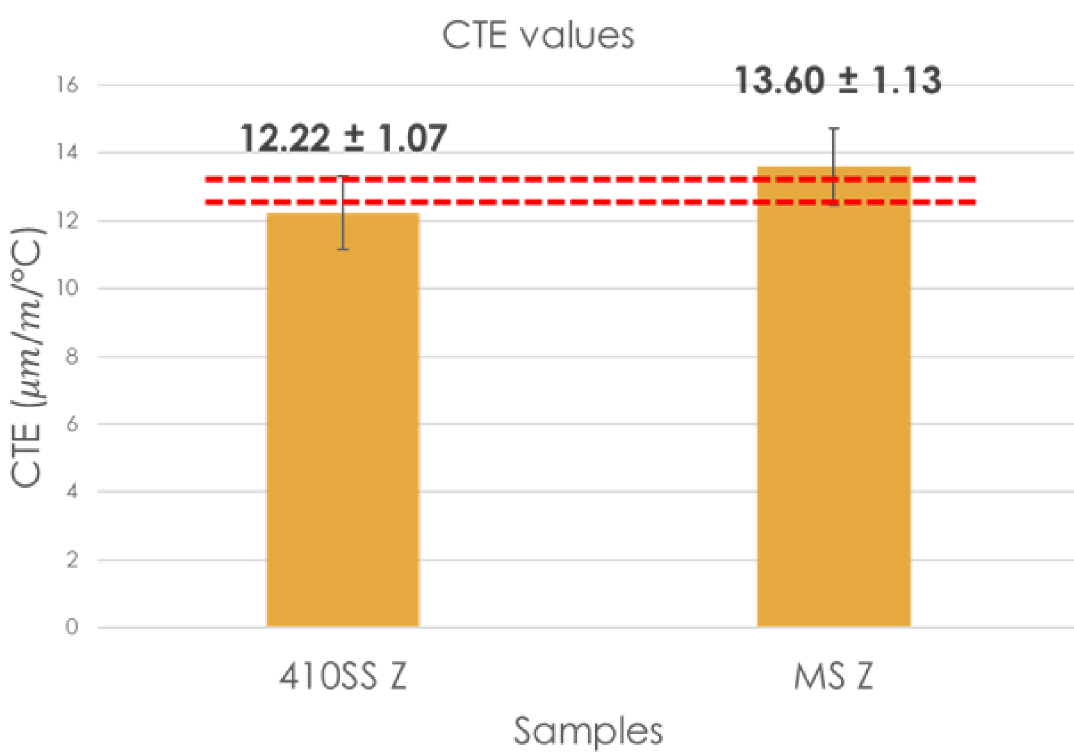

Figure 26: CTE test results

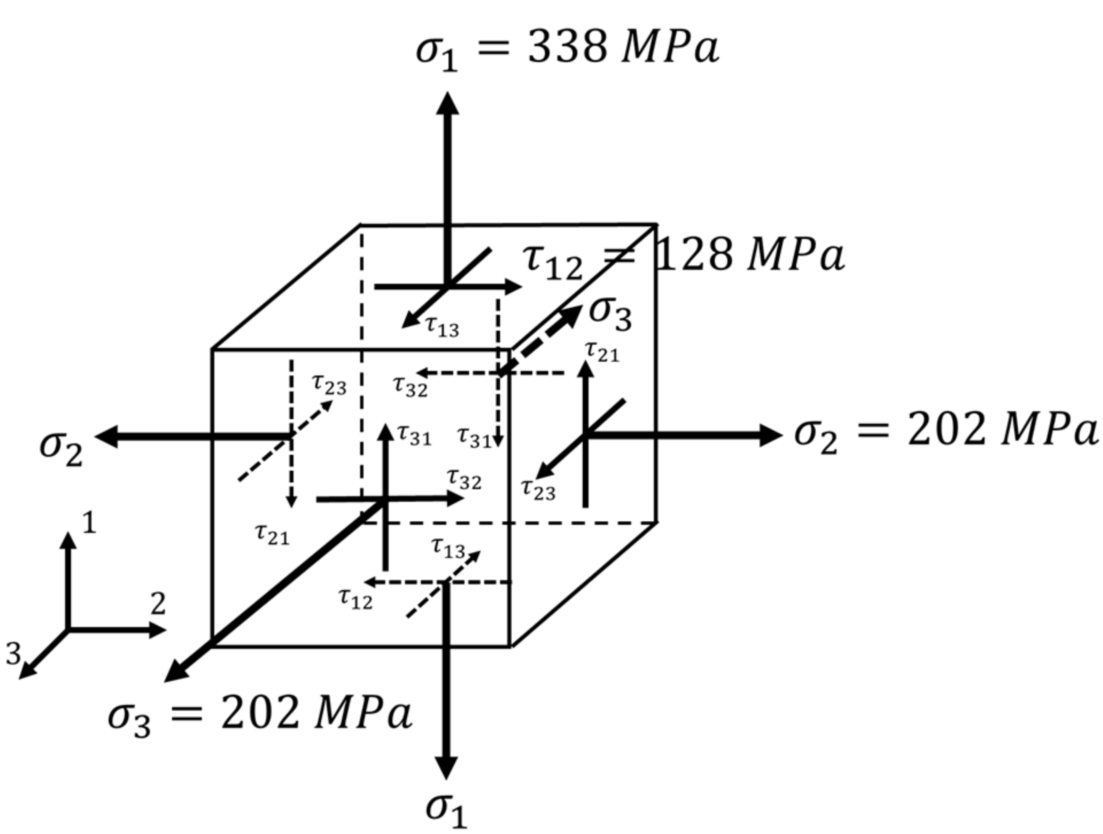

Figure 27: Resolved stress element considering thermal stresses along σ_2 and σ_3

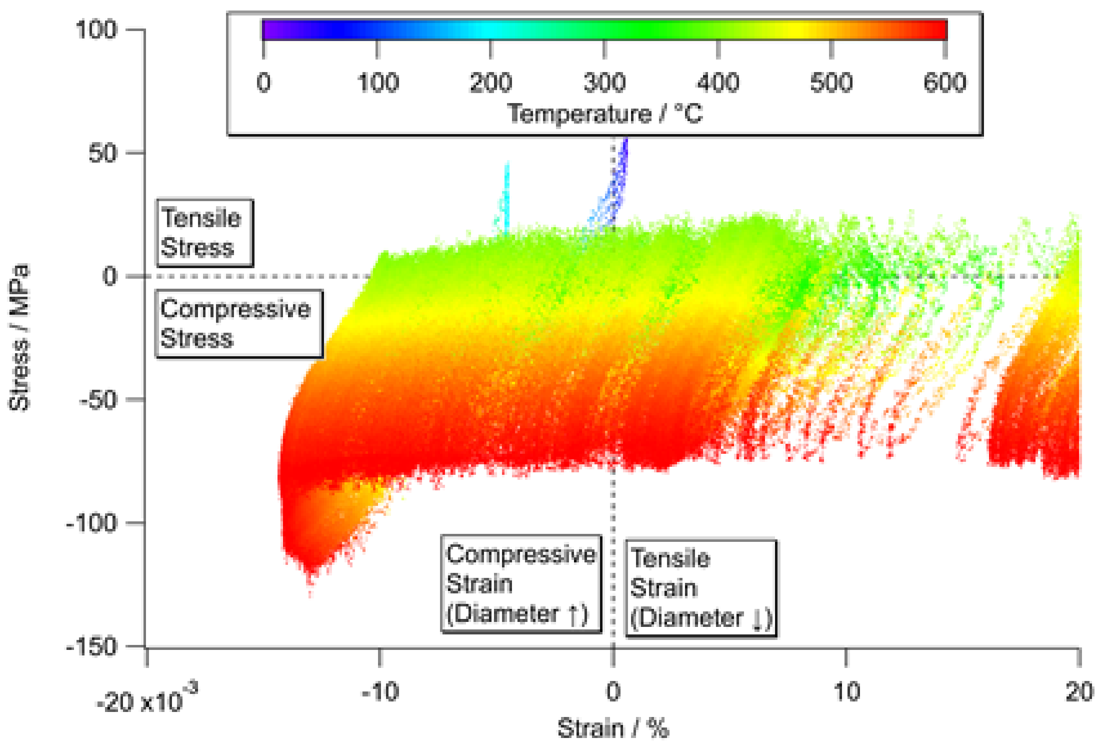

Figure 28: Stress-Strain results plot for sample 1

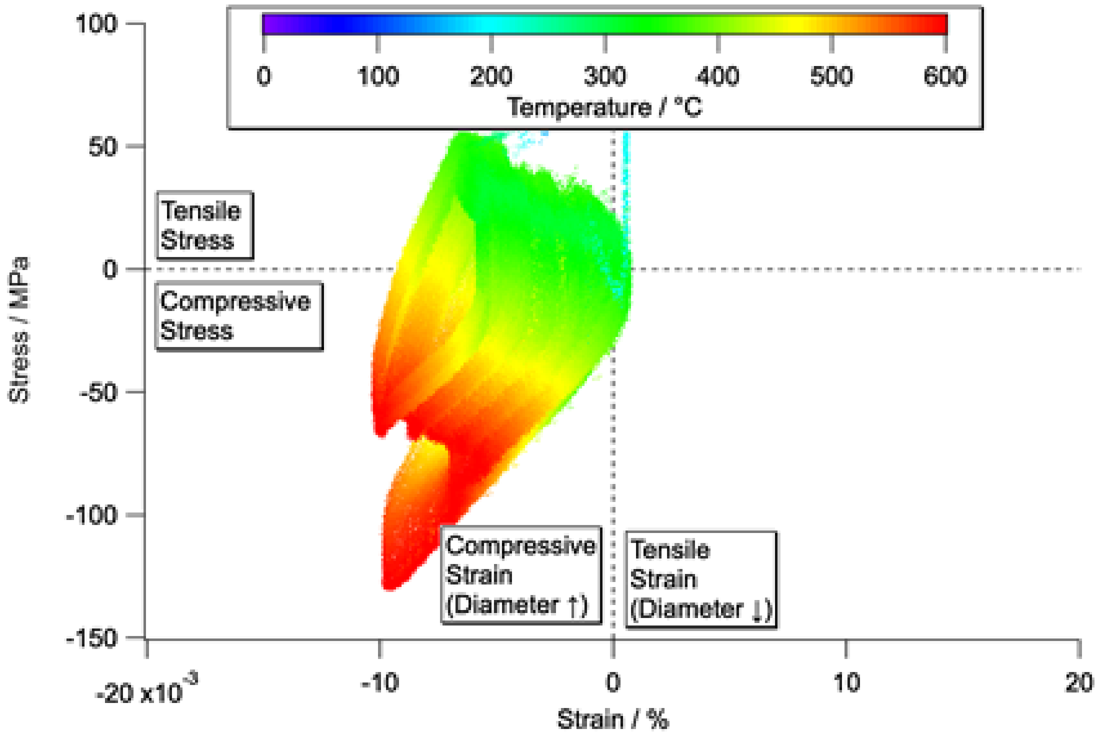

Figure 29: Stress-Strain results plot for sample 2

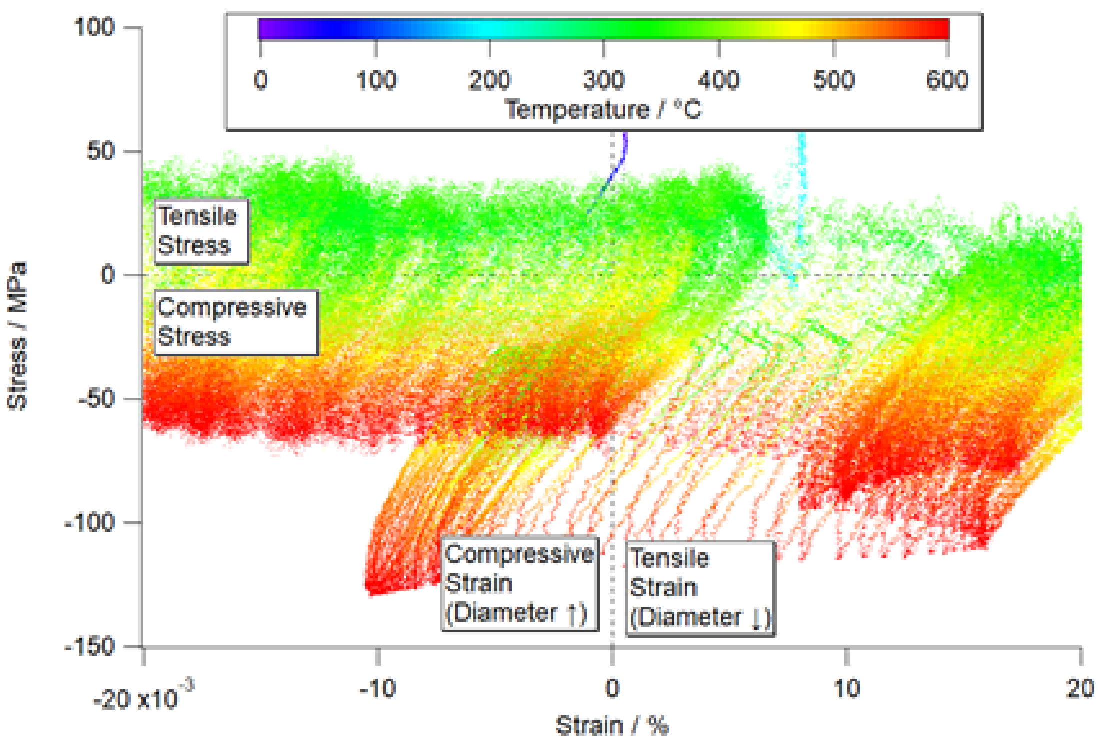

Figure 30: Stress-Strain results plot for sample 3

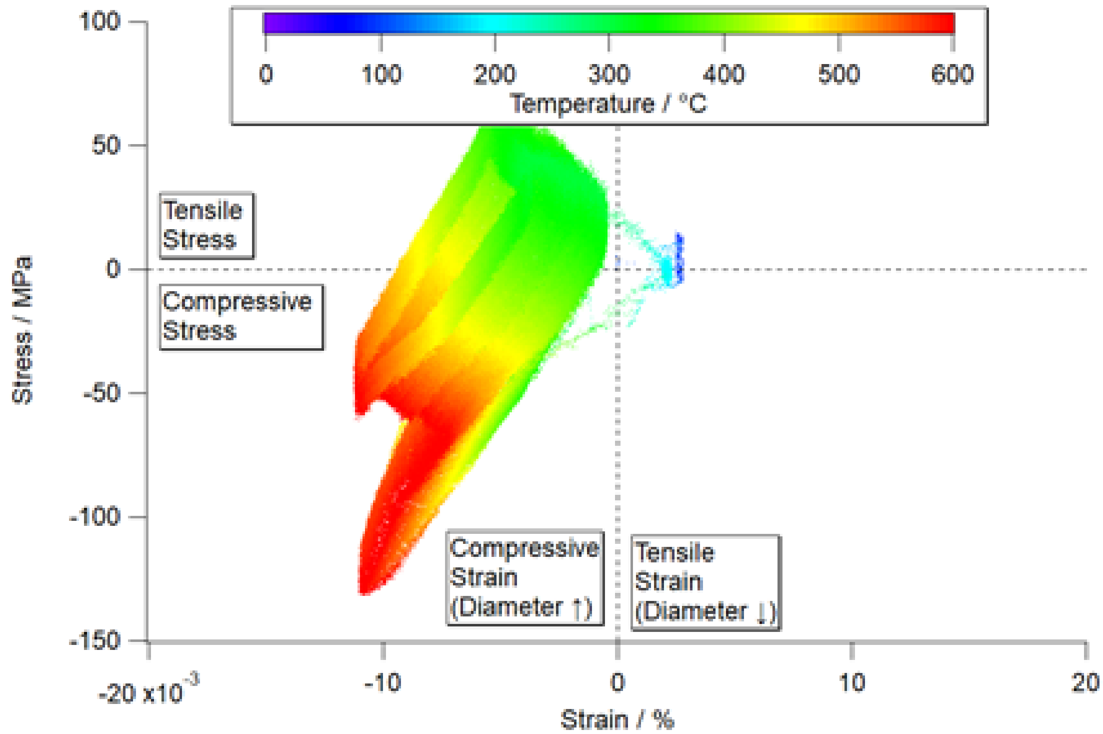

Figure 31: Stress-Strain results plot for sample 4

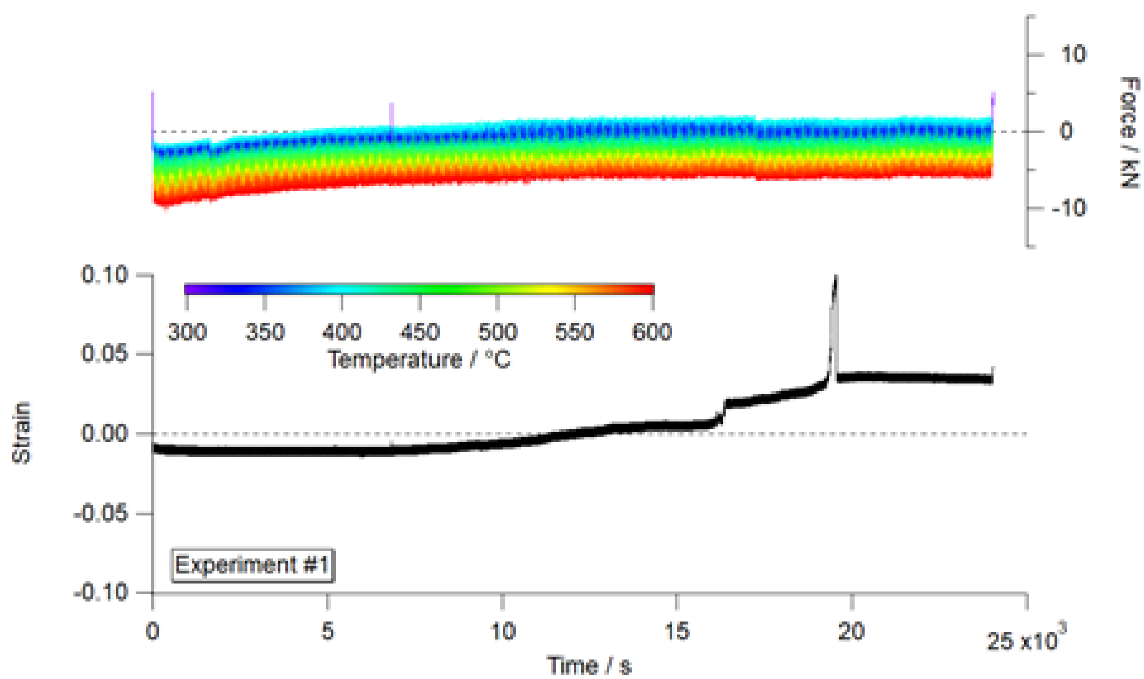

Figure 32: Force-time results plot for sample 1

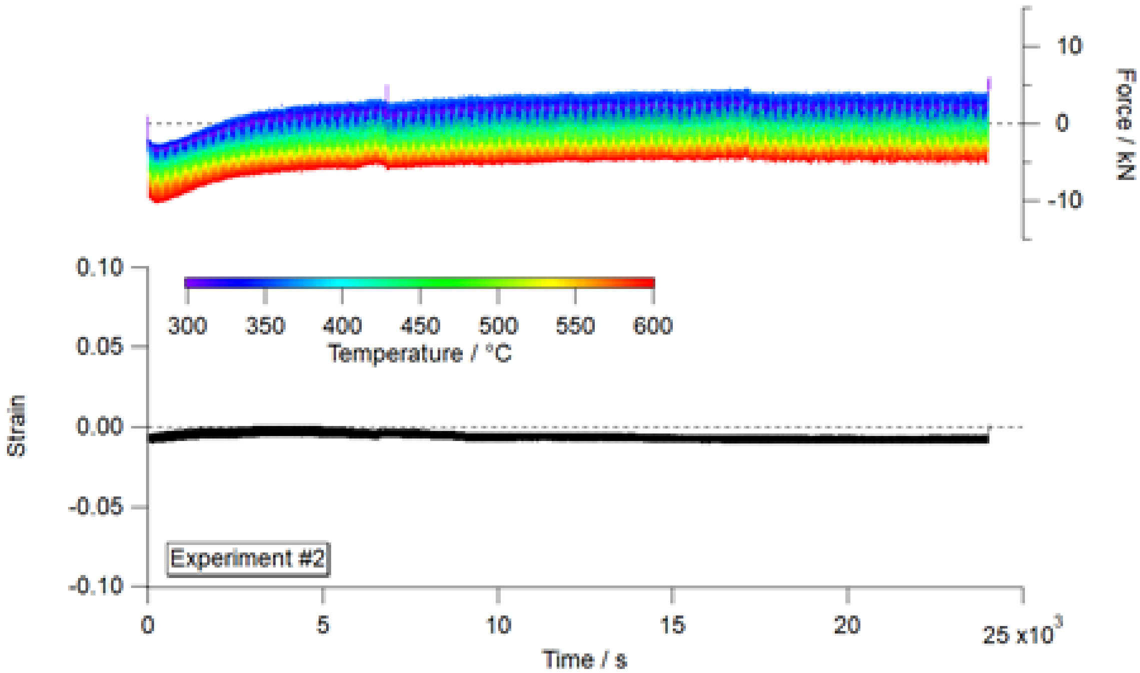

Figure 33: Force-time results plot for sample 2

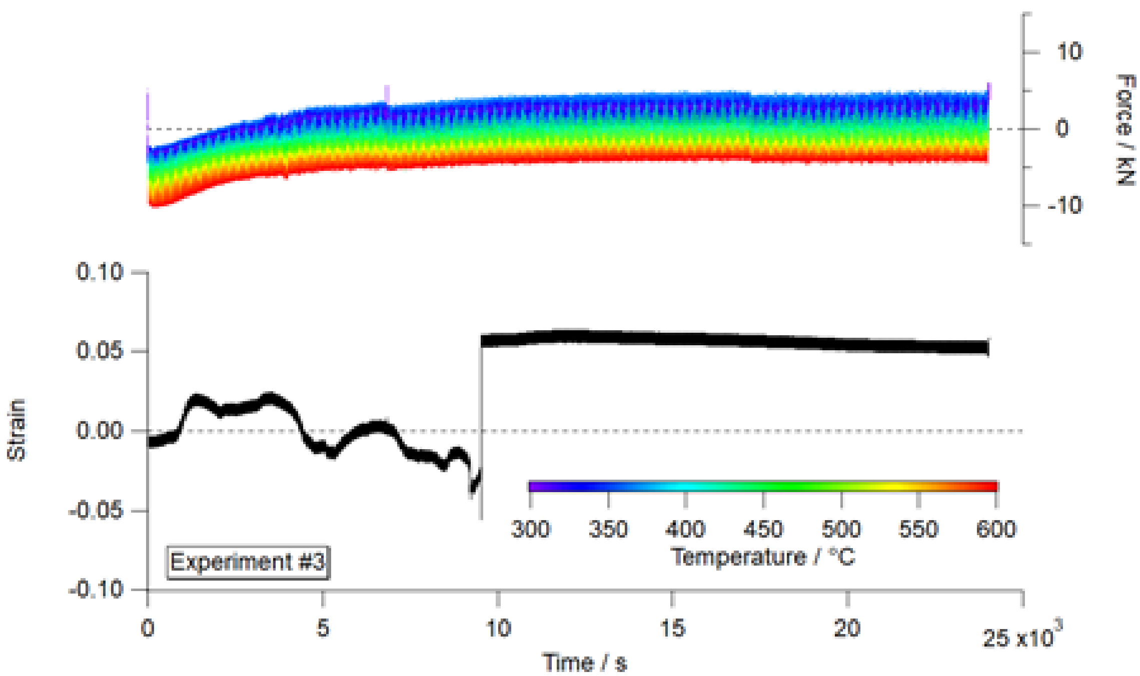

Figure 34: Force-time results plot for sample 3

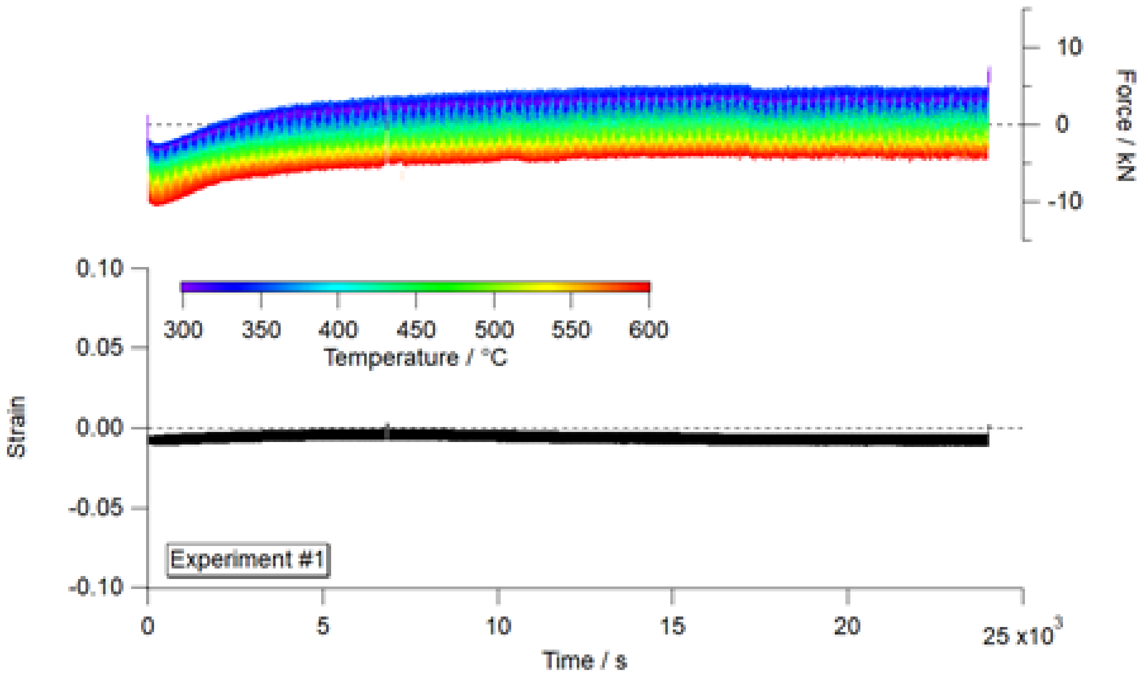

Figure 35: Force-time results plot for sample 4

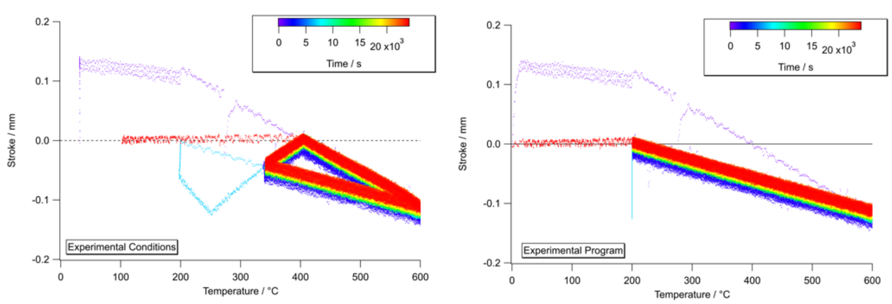

Figure 36: Sample 1 experimental temperature vs programmed temperature profile

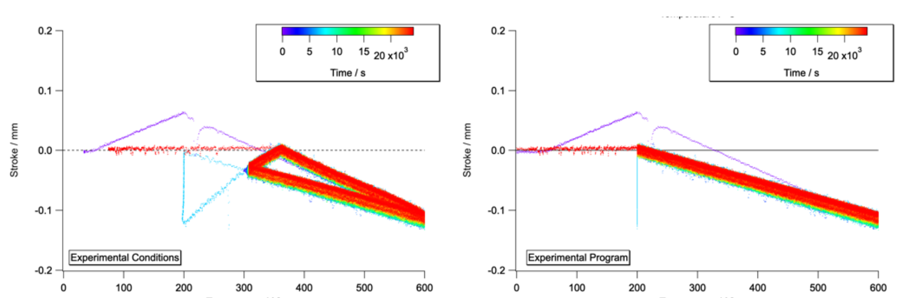

Figure 37: Sample 2 experimental temperature vs programmed temperature profile

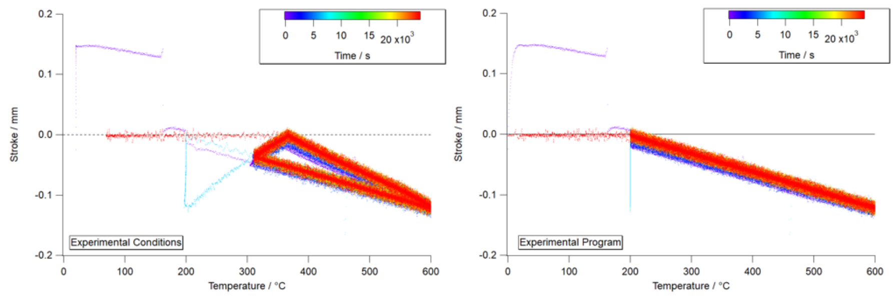

Figure 38: Sample 3 experimental temperature vs programmed temperature profile

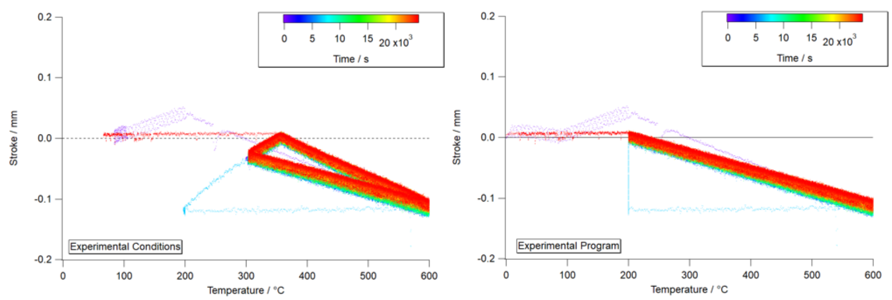

Figure 39: Sample 4 experimental temperature vs programmed temperature profile

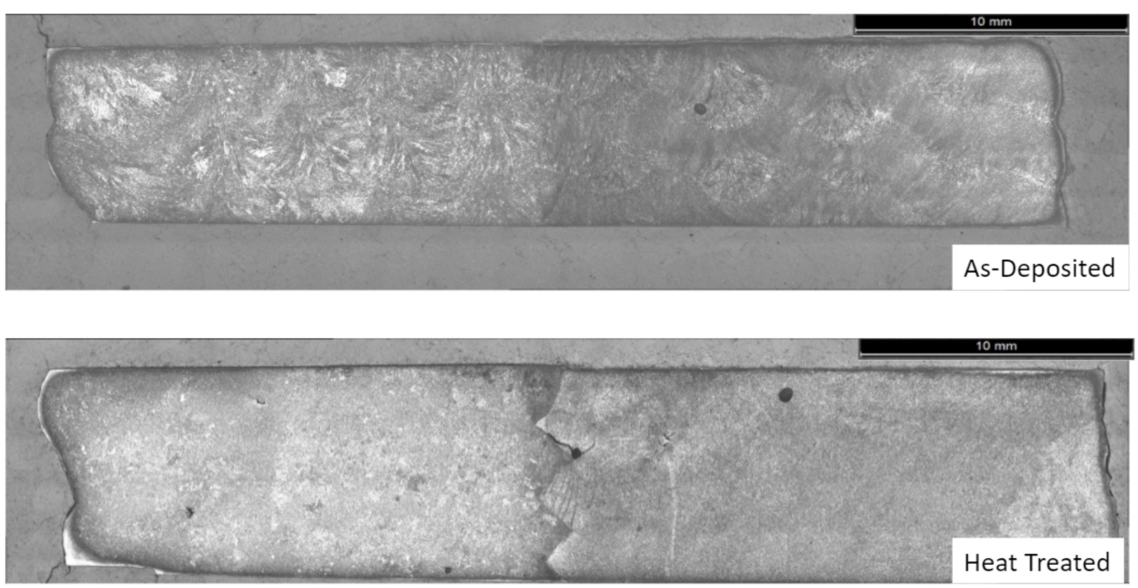

Figure 40: Microstructure comparison between as-printed sample (above) and heat-treated sample (below)

B Figures (cont.)

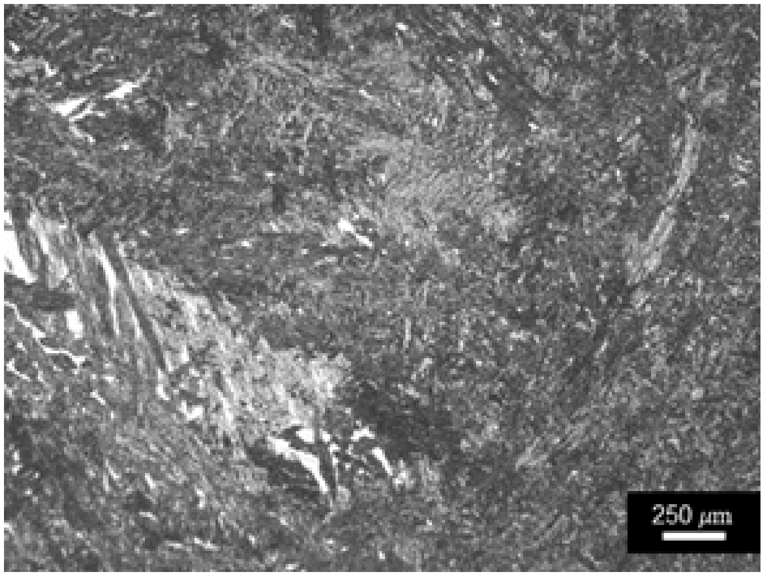

Figure 41: Delta ferrite grains in the as-printed condition

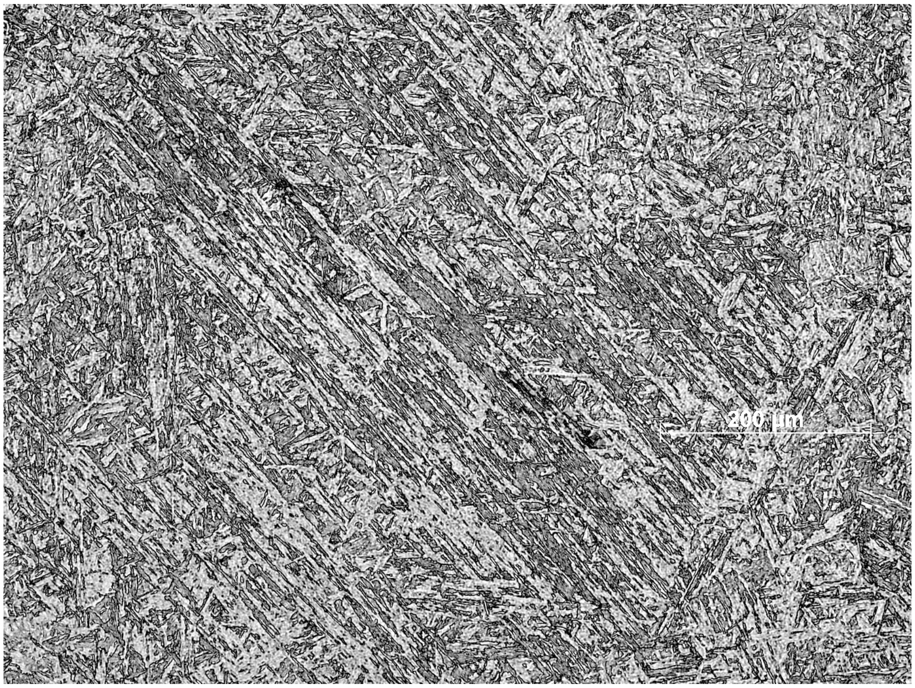

Figure 42: Sample 1 interface region microstructure after fatigue testing at 100x magnification

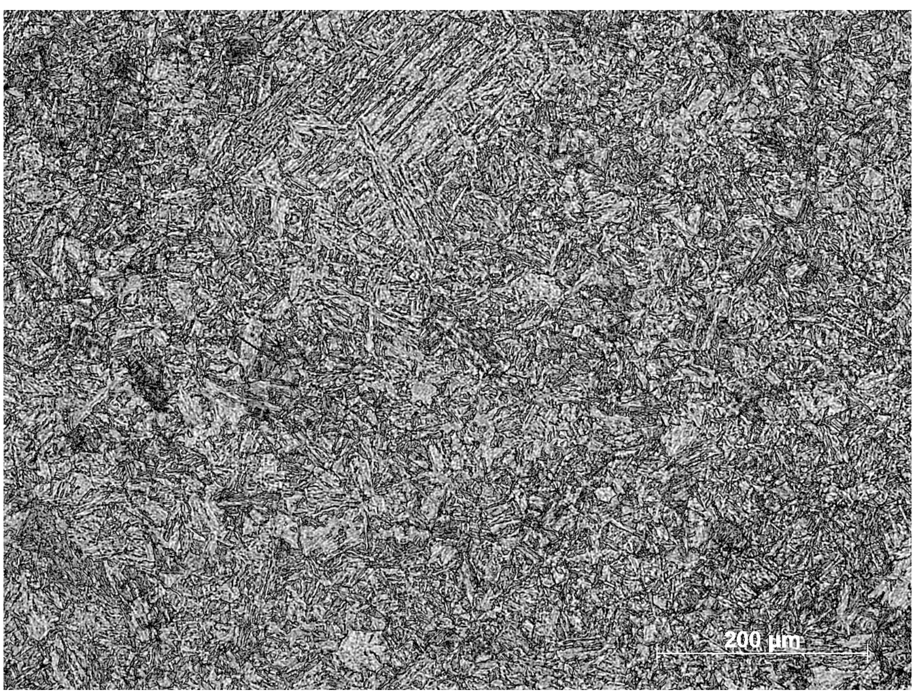

Figure 43: Sample 2 interface region microstructure after fatigue testing at 100x magnification

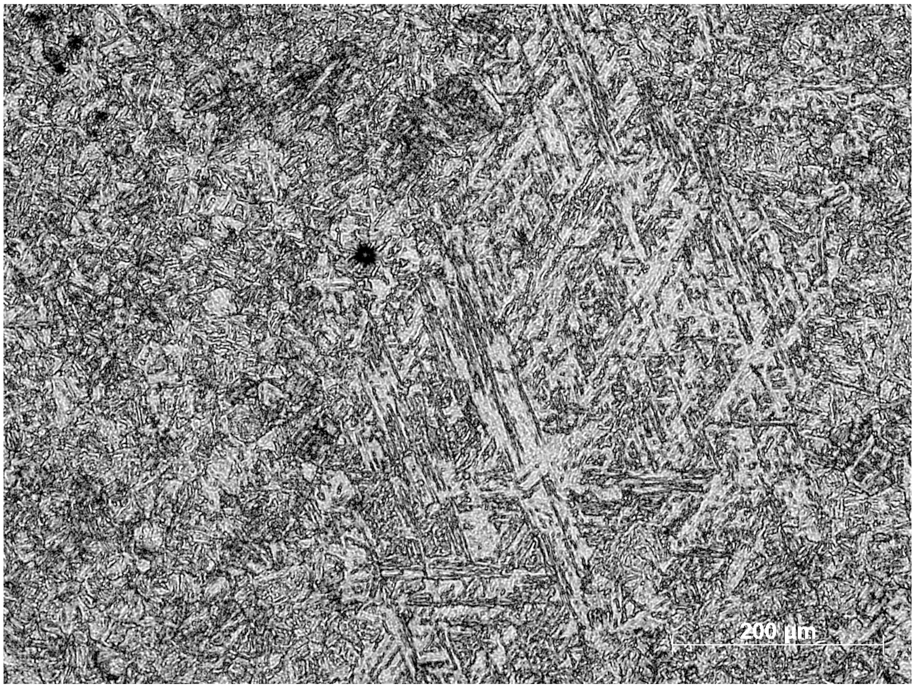

Figure 44: Sample 3 interface region microstructure after fatigue testing at 100x magnification

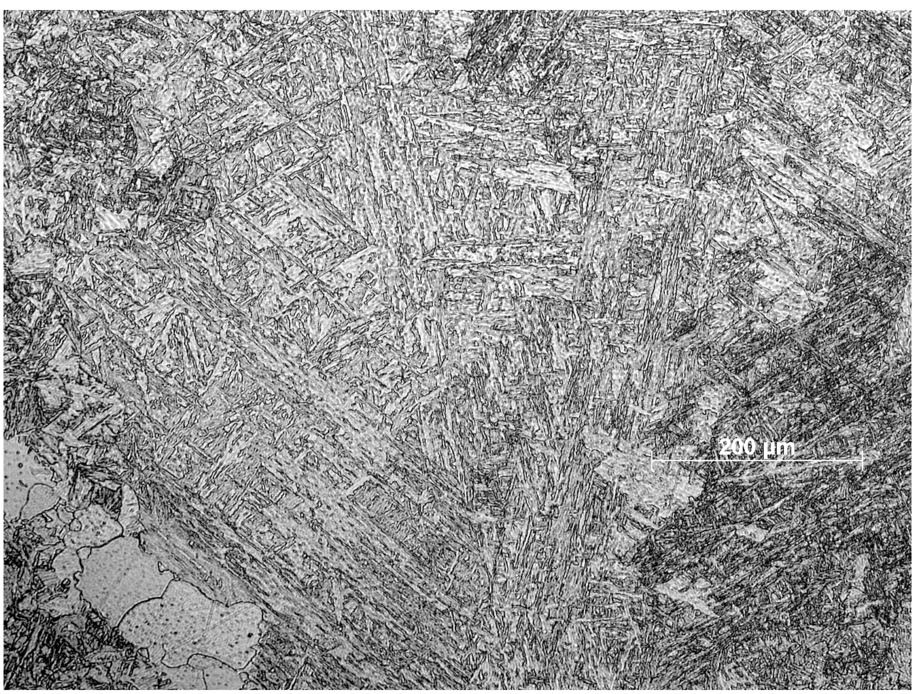

Figure 45: Sample 4 interface region microstructure after fatigue testing at 100x magnification

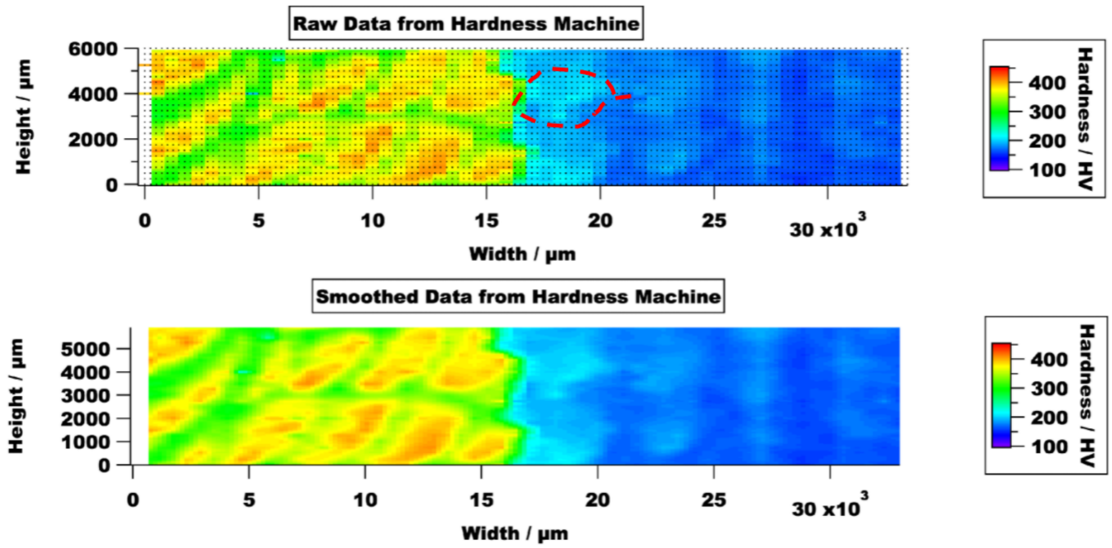

Figure 46: As-printed sample hardness map

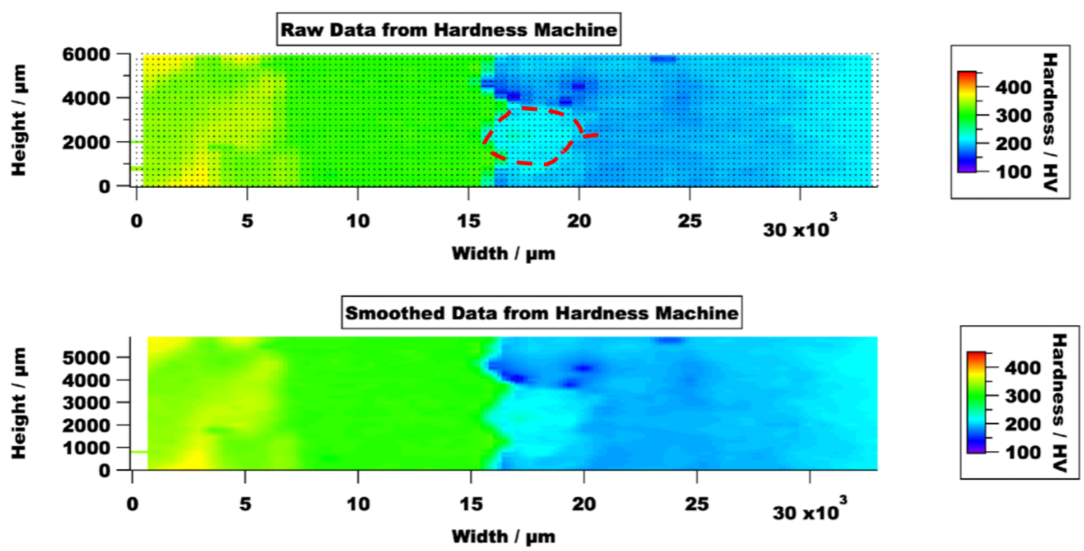

Figure 47: Heat-treated sample hardness map

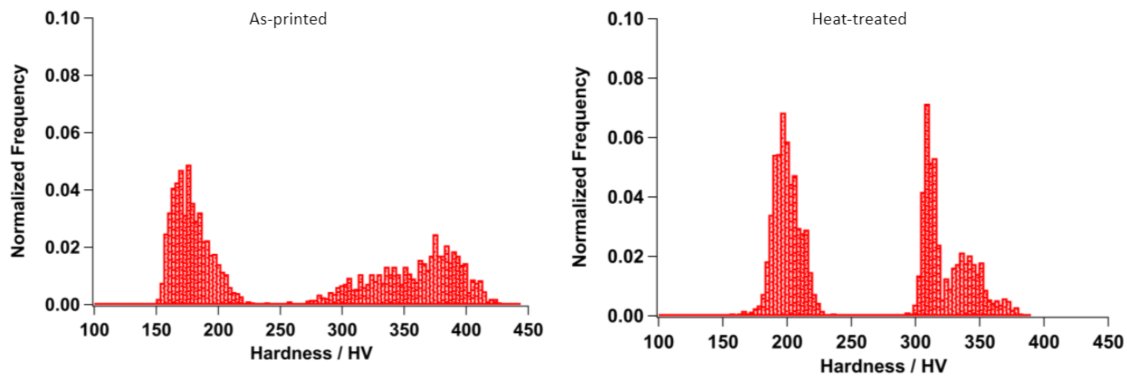

Figure 48: Hardness histogram comparison

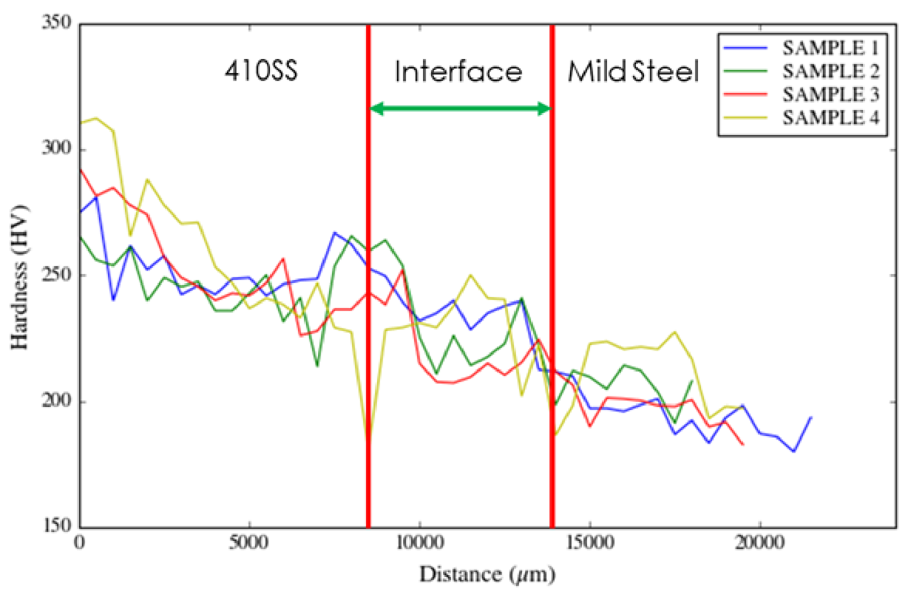

Figure 49: Hardness comparison between tested samples over distance

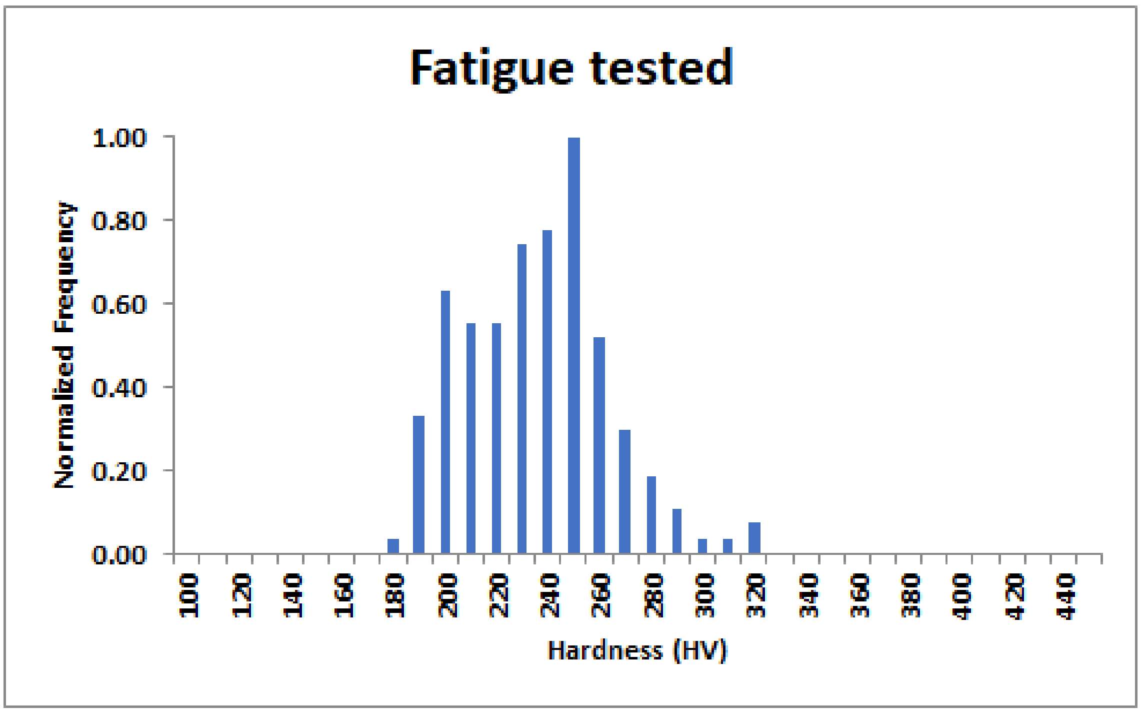

Figure 50: Hardness histogram for fatigue-tested samples

C Tables

Table 1: 22MnB5 composition

C	Mn	Si	Ni	Cr	Cu	S	P	Al
0.221	1.29	0.28	0.13	0.193	0.01	0.001	0.018	0.032
V	Ti	B						
0.005	0.039	0.0038						

Table 2: 410 martensitic stainless steel composition

C	Mn	Si	Ni	Cr	Cu	S	P	Mo	Fe
0.11	0.45	0.39	0.1	12.5	0.14	0.01	0.01	0.03	Bal.

Table 3: Mild steel composition steel composition

C	Mn	Si	Ni	Cr	Cu	S	P	Mo	V	Fe
0.09	1.60	0.09	0.05	0.05	0.20	0.007	0.007	0.05	0.05	Bal.

Table 4: Material Properties

	410SS	MS
Tensile strength @ 25°C	1226 MPa	520 MPa
Yield strength @ 25°C	937 MPa	378 MPa
Tensile strength @ 25°C	490 MPa	150 MPa
Yield strength @ 25°C	375 MPa	110 MPa
Modulus of elasticity @ 25°C	200 GPa	200 GPa
Modulus of elasticity @ 25°C	190 GPa	190 GPa

Table 5: Deposition parameters

Travel speed	40cm/min
Wire Feed Speed	5m/min
410SS Bead Height	4.5mm
SS Bead Width	3.3mm
MS Bead Height	2.3mm
MS Bead Width	4.5mm
SS Bead Overlap	2.4mm
MS Bead Overlap	3.3mm

Vita

After growing up in his hometown Vega Baja, Puerto Rico, Obed Daniel Acevedo Román attended the Inter-American University of Puerto Rico in Bayamón, Puerto Rico, where he received his Bachelor of Science degree in Mechanical Engineering. An Oak Ridge National Laboratory internship made him want to pursue graduate studies at the University of Tennessee, Knoxville. He decided he wanted to pursue a Master of Science degree in Mechanical Engineering, focusing on the mechanical metallurgy of steel systems. His research interests include the mechanical behavior of additively manufactured dissimilar steel systems and mechanical testing. After completing his graduate degree, Obed wishes to pursue a career in industry where he can work in material testing and manufacturing. Obed considers himself fortunate by having the full support of his fiancée and family throughout this exciting time.